Soluble limit and criticality of fermions in $\mathbb{Z}_2$ gauge theories

Elio J. König [1], Piers Coleman,[1,2] and Alexei M. Tsvelik[3]

[1]*Department of Physics and Astronomy, Center for Materials Theory, Rutgers University, Piscataway, New Jersey 08854 USA*
[2]*Department of Physics, Royal Holloway, University of London, Egham, Surrey TW20 0EX, United Kingdom*
[3]*Condensed Matter Physics and Materials Science Division, Brookhaven National Laboratory, Upton, New York 11973, USA*

Quantum information theory and strongly correlated electron systems share a common theme of macroscopic quantum entanglement. In both topological error correction codes and theories of quantum materials (spin liquid, heavy fermion and high-T_c systems), entanglement is implemented by means of an emergent gauge symmetry. Inspired by these connections, we introduce a simple model for fermions moving in the deconfined phase of a $\mathbb{Z}_2$ gauge theory by coupling Kitaev's toric code to mobile fermions. This permits us to exactly solve the ground state of this system and map out its phase diagram. Reversing the sign of the plaquette term in the toric code permits us to tune the ground state between an orthogonal metal and an orthogonal semimetal in which gapless quasiparticles survive despite a gap in the spectrum of original fermions. The small-to-large Fermi surface transition between these two states occurs in a stepwise fashion with multiple intermediate phases. By using a diagrammatic technique, we are able to explore physics beyond the integrable point to examine various instabilities of the deconfined phase and to derive the critical theory at the transition between deconfined and confined phases. We outline how the fermionic toric code can be implemented as a quantum circuit, thus providing an important link between quantum materials and quantum information theory.

I. INTRODUCTION

Strongly correlated quantum materials provide natural occurrence of macroscopic entanglement which is believed to be reflected in a variety of exotic experimental observations: the acclaimed Fermi surface reconstruction without symmetry breaking in cuprates [1] and heavy fermion systems [2]; quantum oscillations in (bulk) insulating YbB_{12} [3] (and arguably also SmB_6 [4,5]); anomalous thermal transport and spin relaxation in spin liquid candidates, e.g., in the organic salt κ-$ET_2Cu_2CN_3$ [6]. All of these materials have the vicinity to (partial) Mott transitions in common (the Kondo breakdown on the lattice can be regarded as an orbital selective Mott localization [7]).

A theoretically appealing approach to such systems involves fractionalized particles and topological order [8]. Strong correlations impose (Gutzwiller-) projected local Hilbert spaces. These can be treated in prefractionalized slave-boson [9] or slave-spin [10,11] theories, whereby a gauge symmetry [typically U(1), SU(2), or $\mathbb{Z}_2$] is introduced. Topological order enters through the physics of these lattice gauge theories. In particular, sufficiently large space-time dimensions sustain deconfined states, i.e., macroscopically entangled superposition states with Wegner-Wilson loops of any length and topological ground-state degeneracy on tori.

Topological order is crucial to explain the Fermi-surface reconstruction without symmetry breaking [12]. Conventionally, the Fermi-surface volume is fixed by the total electron density [13,14] (including f electrons for Kondo lattices).

However, topological order exploits a loophole [15,16] in the derivation of the Luttinger-Oshikawa theorem.

The same macroscopic entanglement associated with topological order is also utilized in quantum error correction codes. For example, Kitaev's soluble toric code model [17] interweaves numerous imperfect physical qubits to two robust logical qubits. We here exploit this insight from quantum information science and expose the toric code to a fermionic bath, Fig. 1(a): We thereby obtain asymptotically exact analytical results about deconfined states of gauge theories coupled to itinerant electrons. Additionally, we extend previous toric-code proposals to design an analog quantum computer of fermionic $\mathbb{Z}_2$ gauge theories, Fig. 6.

Recently, there has been substantial numerical progress in the study of deconfinement in metals [18–24]. Certain fermionic $\mathbb{Z}_2$ gauge theories are amenable to quantum Monte-Carlo methods (sign-free) and provide evidence for small-to-large Fermi surface transitions without symmetry breaking [22–24]. Despite this, numerically realistic system sizes and the pertinent obstacle of analytical continuation in frequency space are still a limitation in resolving sharp Fermi-surface features. Complementary techniques which overcome such problems, in particular, simple analytically tractable models of fermions in deconfined gauge theories [25] are widely lacking. A promising approach [26,27] is to Kondo couple conduction fermions to the simplest exactly soluble spin liquid with deconfined $\mathbb{Z}_2$ gauge degrees of freedom—Kitaev's honeycomb model [28]. However, to the best of our knowledge, only perturbative or mean-field results are available to date.
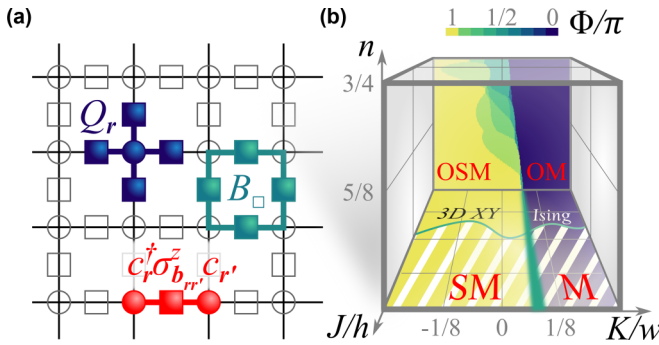
FIG. 1. (a) Graphical illustration of the mutually commuting operators in the fermionic toric code, Eq. (1). (b) Phase diagram [(O)M = (orthogonal) metal, (O)SM = (orthogonal) semimetal] as a function of coupling constants K/w, J/h and filling n. Numerical data in the $J = 0$ plane (in the back) is combined with a schematic illustration for $J > 0$.

In this paper, we introduce a simple model of fermions in the deconfined (i.e., topological) phase of $\mathbb{Z}_2$ gauge theory—a fermionic toric code [17,29–32], see Eqs. (1) below and Fig. 1(a). We begin our discussion from the asymptotic cases $K \gg w$ [$K \ll -w$] in the phase diagram Fig. 1(b), when the ground state is easily determined to be an orthogonal metal (OM) [orthogonal semimetal (OSM)] with large [small] Fermi surface. We are able to characterize the small to large Fermi-surface transition as an infinite sequence of symmetry broken states with fractional average flux Φ and develop a diagrammatic technique to systematically include perturbations about this soluble point and to study the transition to the confined phase.

The OM concept was introduced in Ref. [33] as a state similar to a normal metal in all respects (e.g., conductivity and thermodynamics) except for the behavior of single-electron Green's functions (e.g., the spectral function is gapped). In Ref. [33], the lattice fermions were fractionalized into "orthogonal" fermions and slave spins $c_{\mathbf{r},\alpha} \rightarrow \tau_{\mathbf{r}}^z f_{\mathbf{r},\alpha}$, where $\tau_{\mathbf{r}}^a$ are Pauli matrix operators. In the OM, the τ spins are disordered, while the f fermions are in a Fermi-liquid state. The authors of Ref. [33] provided exemplary solvable models. Recently, the authors of Ref. [23] introduced a model of OM as a $\mathbb{Z}_2$ gauge theory where τ spins played the role of Higgs bosons.

Here we suggest a radical simplification of the theory by generalizing the mapping between the toric code and $\mathbb{Z}_2$ gauge theory [34,35]. The explicit application of Gauss's law removes the necessity of f fermions and Higgs bosons and enables us to work with gauge-invariant fermions (see Appendix A for details), which extends our calculational capacities. The exact solution of the resulting fermionic toric code and associated diagrammatics play the same role as free fermions in ordinary metals, providing the starting point for perturbation theory and a positive definition of a ($\mathbb{Z}_2$-deconfined) non-Fermi liquid as the class of quantum states of nonintegrable models which are adiabatically connected to the ground state of the soluble model.

II. BARE MODEL

The soluble starting point for our discussions is a generalization of Kitaev's toric code [17] by means of fermionic matter fields. The basic Hamiltonian $H_0 = H_K + H_h + H_c$ is given by

$$H_K = -K \sum_{\square} B_{\square}, \quad H_h = -h \sum_{\mathbf{r}} Q_{\mathbf{r}}, \quad (1a)$$

$$H_c = -w \sum_{\langle \mathbf{r},\mathbf{r}' \rangle} \sigma_{\mathbf{b}_{\mathbf{r},\mathbf{r}'}}^z c_{\mathbf{r},\alpha}^\dagger c_{\mathbf{r}',\alpha} - \mu \sum_{\mathbf{r}} c_{\mathbf{r},\alpha}^\dagger c_{\mathbf{r},\alpha}. \quad (1b)$$

Here, $c_{\mathbf{r},\alpha}^\dagger$ creates a fermion with spin component $\alpha = \uparrow, \downarrow$ at a vertex $\mathbf{r}$ of a square lattice [depicted by circles in Fig. 1(a)], while $\mathbb{Z}_2$ gauge fields are represented by Pauli matrices $\sigma_{\mathbf{b}}^a$ ($a = x, y, z$) located on each bond $\mathbf{b}$ [depicted by squares in Fig. 1(a)]. The flux (= plaquette) operators $B_{\square} = \prod_{\mathbf{b} \in \square} \sigma_{\mathbf{b}}^z$ and charge (= star) operators $Q_{\mathbf{r}} = (-1)^{\hat{n}_{\mathbf{r}}} \prod_{\mathbf{b} \in +_{\mathbf{r}}} \sigma_{\mathbf{b}}^x$ (where $\hat{n}_{\mathbf{r}} = \sum_{\alpha} c_{\mathbf{r},\alpha}^\dagger c_{\mathbf{r},\alpha}$) all mutually commute, and moreover commute with the fermionic term H_c (we assume $w > 0$). In distinction to a model studied in Refs. [32,36–38], in Eqs. (1) a factor $(-1)^{\hat{n}_{\mathbf{r}}}$ is included into $Q_{\mathbf{r}}$ which allows the following projective construction of the ground state.

A. Ground states for $|K/w| \gg 1$

As in the toric code, the construction of the ground state $|\text{GS}\rangle$ of Eqs. (1) relies on an extensive number of integrals of motion $B_{\square}$, $Q_{\mathbf{r}}$ with eigenvalues ± 1. We first consider the limit $|K/w| \gg 1$ in which all ground states are homogeneous with zero flux (π flux), $B_{\square} |\text{GS}_0\rangle = |\text{GS}_0\rangle$ ($B_{\square} |\text{GS}_\pi\rangle = -|\text{GS}_\pi\rangle$), through all plaquettes. It is illustrative to first set $h = 0$. In this limit, $\sigma_{\mathbf{b}}^z$ are classical variables and we choose a gauge in which the gauge sector of the zero-flux (π-flux) solution, denoted $|0\rangle_\sigma$ ($|\pi\rangle_\sigma$), suffices $\langle \sigma_{\mathbf{b}}^z \rangle = 1$ ($\langle \sigma_{\mathbf{b}}^z \rangle = (-1)^{b_x}$). Then, the fermionic term H_c can be readily solved by Fourier transform. Of course, the dispersion is different in the zero flux [$\epsilon_0(\mathbf{k}) = -w(\cos(k_x) + \cos(k_y))$; $\mathbf{k} \in (-\pi, \pi) \times (-\pi, \pi)$] and π-flux background [$\epsilon_\pi^\pm(\mathbf{k}) = \pm w \sqrt{\cos^2(k_x) + \cos^2(k_y)}$; $\mathbf{k} \in (-\pi/2, \pi/2) \times (\pi, \pi)$]. In either case, the ground state in the fermionic sector is a Fermi sea which we denote $|\text{FS}_{0/\pi}\rangle_c$. The re-imposition of $h > 0$ requires $Q_{\mathbf{r}} |\text{GS}\rangle = |\text{GS}\rangle$ ($\forall \mathbf{r}$). This lifts the macroscopic degeneracy of candidate ground states, leaving only two contenders in the infinite plane,

$$|\text{GS}_0\rangle = \prod_{\mathbf{r}} \hat{P}_{\mathbf{r}}[|\text{FS}_0\rangle_c |0\rangle_\sigma], \quad E_0 = -K - h + 2E_{c,0}, \quad (2a)$$

$$|\text{GS}_\pi\rangle = \prod_{\mathbf{r}} \hat{P}_{\mathbf{r}}[|\text{FS}_\pi\rangle_c |\pi\rangle_\sigma], \quad E_\pi = K - h + 2E_{c,\pi}, \quad (2b)$$

where $\hat{P}_{\mathbf{r}} = (1 + Q_{\mathbf{r}})/2 = \hat{P}_{\mathbf{r}}^2$. These two states represent superpositions of configurations of σ fields which preserve the flux configuration. The fermion dispersion, denoted $\epsilon_0(\mathbf{k})$ [$\epsilon_\pi(\mathbf{k})$], of these phases enable us to identify $|\text{GS}_0\rangle$ [$|\text{GS}_\pi\rangle$] as an OM [OSM], respectively. We emphasize that, despite the inhomogenous gauge-field configuration and the small semimetallic Fermi surface, $|\text{GS}_\pi\rangle$ breaks neither crystalline symmetries (the latter being projectively represented, see Appendix B) nor the Oshikawa-Luttinger theorem (because the gauge sector is deconfined, see Appendix C) [16].

B. Small to large Fermi surface transition

While it is clear that the eigenstates presented in Eqs. (2) yield the correct ground state for $|K/w| \gg 1$, inhomogenous states displaying arrays of π fluxes with density $\Phi \neq 0, \pi$ become important at small $|K/w|$. These are not favorable for H_K, but yield energetic gain of order w by lowering the ground state of the electrons. The latter effect is especially great when the band is at commensurate (e.g., half) filling due to the nesting of the Fermi surface. Indeed [32], Monte Carlo simulations corroborate the conjecture that the average flux density at $K = 0$ and filling n is $\Phi = 2\pi n$. The situation is somewhat similar to the quantum Hall effect with its succession of various quantum Hall states [39].

For a given flux density Φ, it is reasonable to assume that the ground-state configuration is given by some regular array of π fluxes. For each of these, a ground state $|GS_\Phi\rangle = \prod_r \hat{P}_r[|FS_\Phi\rangle_c |\Phi\rangle_\sigma]$ can be readily constructed and the ground-state energy determined. Contrary to the OM and OSM, the intermediate states do break crystalline symmetries, even when represented projectively. This is revealed in the ground-state averages of the $B_\square$ operators which are invariant under action of the projection operators. Therefore, we expect that the OM-OSM transition, which separates distinct gapless quantum phases characterized by different projective representation of translations [23], occurs as an infinite succession of symmetry broken states with fractional average flux $\Phi = \pi k/N_\Phi$ ($k = 1, \ldots, N_\Phi - 1$).

To substantiate this hypothesis, we have semianalytically investigated a large variety of trial flux configurations for $N_\Phi = 8$. While we relegate technical details to Appendix G, we here illustrate the procedure and consider two exemplary states with average flux $\Phi = \pi/2$: an arrangement of vertical lines and a checkerboard pattern. The corresponding eigenvalues E are determined by

$$4 - \cos(4k_x) + 8(E^2 - 2)E^2 + (4 - 8E^2)\cos(2k_y)$$
$$+ \cos(4k_y) = 0 \quad \text{(vertical stripes)}, \tag{3a}$$

$$2 - 4\sin(2k_x)\sin(2k_y) - \cos(4k_x) + 8(E^2 - 2)E^2$$
$$- \cos(4k_y) = 0 \quad \text{(checkerboard)}. \tag{3b}$$

The configurations and corresponding band structures are presented in Fig. 2. In particular, for the checkerboard pattern there are four Dirac points in the Brillouin zone. The ground-state energy as a number of filling is readily obtained for these two configurations and within the $\pi/2$ sector, the stripy (checkerboard) pattern is favorable near half (quarter) filling, see Appendix G. We repeat the procedure for ~ 30 other trial states and represent the flux density associated with lowest energy as a color plot in Fig. 1(b). As the stepsize $1/N_\Phi \to 0$, the observed succession of states is expected to coalesce into a quantum phase transition with a finite, critical, strange metallic region.

C. Excitations

We return to the OM and OSM phases, for which fermionic single-particle excitations are

$$|e : \mathbf{k}\rangle = \prod_r \hat{P}_r[c_\mathbf{k}^\dagger |FS_{0/\pi}\rangle_c |0/\pi\rangle_\sigma], \quad \mathbf{k} \notin \text{Fermi sea}, \tag{4a}$$

$$|h : \mathbf{k}\rangle = \prod_r \hat{P}_r[c_\mathbf{k} |FS_{0/\pi}\rangle_c |0/\pi\rangle_\sigma], \quad \mathbf{k} \in \text{Fermi sea}. \tag{4b}$$
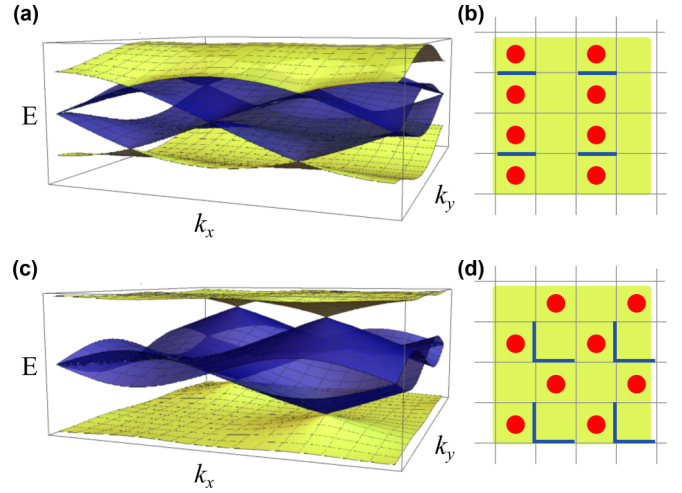

FIG. 2. Band structure associated to flux configurations with average flux $\Phi = \pi/2$ and (a) stripy and (c) checkerboard arrangement of fluxes. Within a unit cell (yellow square), the latter are presented in (b), (d): a π flux is depicted by a red dot, we choose a gauge in which sign(w) is reversed on highlighted bonds.

Electrons (holes) have excitation energy $\epsilon_{0/\pi}(\mathbf{k}) - \mu$ [$\mu - \epsilon_{0/\pi}(\mathbf{k})$] above the ground state. Particle-hole pairs and multifermion excitations can be expressed analogously by insertion of fermionic operators to the right of all projectors $\hat{P}_r$. In contrast to these gapless excitations, states obtained by applying fermionic operators to the left of projectors are gapped, because fermion operators anticommute with Q_r and thus create a local excitation with energy $2h$. Electric strings $W_{\gamma_{r,r'}}^{(e)} = \prod_{\mathbf{b} \in \gamma_{r,r'}} \sigma_\mathbf{b}^z$ along a contour $\gamma_{r,r'}$ also create the same local excitations. As in the toric code, strings are deconfined and have energy $2h$ at each end (this motivates the notion of e particles). However, unlike the toric code, magnetic strings $W_{\gamma_{\square,\square'}^*}^{(m)} = \prod_{\mathbf{b} \in \gamma_{\square,\square'}^*} \sigma_\mathbf{b}^x$ along a dual contour $\gamma_{\square,\square'}^*$ do not create static eigenstates.

D. Diagrammatic technique

Despite the absence of a Wick theorem in the toric code sector, the presence of Wick's theorem for fermions in a Fermi sea allows us to develop a Feynman diagrammatic representation of imaginary time-ordered ground-state correlators of fermionic operators and of σ^z insertions (see Fig. 3 and Appendix D). In distinction to ordinary diagrammatics, a fermion operator inserts a vertex of a local gapped propagator and a dispersive, orthogonal fermion. This is because $c_r^\dagger$ and c_r create an e particle in addition to a fermionic excitation. Similarly, $\sigma_\mathbf{b}^z$ inserts a vertex connecting two e particles at sites adjacent to the bond $\mathbf{b}$. The absent Wick theorem implies nontrivial (but computable) interactions of e particles on sites with more than two vertices.

The simplest correlator—the two-point Green's function, Fig. 3(b)—is $G(\mathbf{r}_1, \mathbf{r}_2; \tau) = \delta_{\mathbf{r}_1, \mathbf{r}_2} e^{-2h|\tau|} G_{FS}(\mathbf{r}_1, \mathbf{r}_1; \tau)$ or in frequency domain

$$G(\mathbf{r}_1, \mathbf{r}_1; z) = \int (dk) \frac{1}{z - \epsilon_0(\mathbf{k}) + \text{sign}[\epsilon_0(\mathbf{k})]2h}. \tag{5}$$
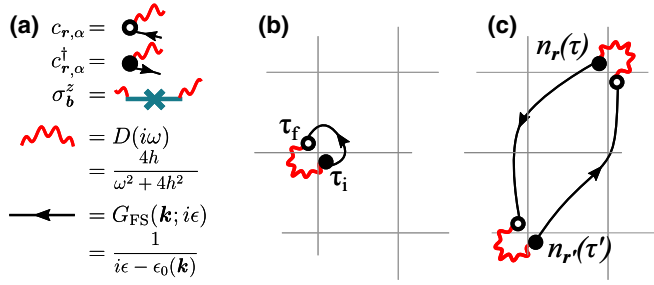
FIG. 3. (a) Diagrammatic representation of operators and bare propagators (here for the OM phase). (b) While the fermionic Green's function is gapped, operator insertions with an even number of fermionic fields at the same space-time position (e.g., density) display ordinary Fermi-liquid behavior because $D(\tau = 0) = 1$. (c) This holds in particular for the polarization operator.

This determines a gapped density of states. On the other hand, the correlators of local two-fermion operators (e.g., the polarization operator) display standard Fermi-liquid behavior, Fig. 3(c). Thus, Eqs. (1) provide a realization of an OM [33]. As a corollary, the instability of the OM (OSM) with respect to any fermionic interaction with local space-time operators, $H_{\text{int}} = \sum_{r,r'} c^\dagger_{r,\alpha} c_{r,\beta} c^\dagger_{r',\alpha'} c_{r',\beta'} V_{\alpha,\beta;\alpha',\beta'}(r,r')$, is exactly the same as in the corresponding confining (i.e., trivial) Fermi liquid phase.

While we have followed the current convention [19,23,33] by considering $c^\dagger_r$ as the creation operator of the physical fermion, following Dirac [40] we could equally have identified $\tilde{c}^\dagger_r = W^{(e)}_{\gamma_{\infty,r}} c^\dagger_r$ as the physical creation operator. This operator simultaneously creates fermions and the associated distortion in the gauge field. It is this object that creates the gapless excitations in Eqs. (4).

III. PERTURBATION THEORY

The diagrammatic technique allows the systematic study of perturbations which break local charge conservation $[\delta H, Q_r] \neq 0$:

$$\delta H = -\sum_{r,r'} t_{r,r'} c^\dagger_{r,\alpha} c_{r',\alpha} - J \sum_b \sigma^z_b. \quad (6)$$

Perturbative contributions in $t_{r,r'}$ (represented by a dashed line) to the Green's function are depicted in Fig. 4, which also illustrates the string tension J of electric strings (we leave a finite string tension of magnetic strings for future studies). In the dual formulation of an Ising-Higgs gauge theory, J represents the nearest-neighbor $\mathbb{Z}_2$ slave-spin interaction.

A. Long-range hopping

An infinite-order resummation of the hopping in the random phase approximation (RPA) becomes justified for long-range $t_{r,r'}$: In all diagrams except Fig. 4(a), t_{r_i,r_f} is multiplied by the Green's functions connecting the same sites. The decay of $G_{\text{FS}}(r_f, r_i; \tau_f, \tau_i)$ in space removes the singularity of the Fourier transform in momentum space. This validates the omission of this kind of diagram in RPA and thus

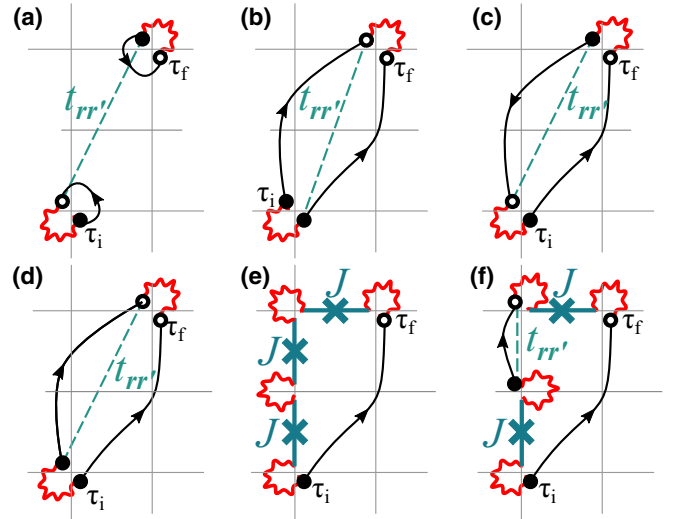$$G_{\text{RPA}}(\boldsymbol{k}, z) = [G(\boldsymbol{x}, \boldsymbol{x}; z)^{-1} + t(\boldsymbol{k})]^{-1}. \quad (7)$$

FIG. 4. Diagrammatic representation of perturbative t and J corrections to $G(r_f, r_i; \tau_f, \tau_i)$. (a)–(d) First-order diagrams in t. (e)–(f) Diagrams contributing to the Higgs transition.

This implies the appearance of dispersive subgap states at energy $E(\boldsymbol{k})$. For example, for the OM phase and constant density of states, $G(\boldsymbol{x}, \boldsymbol{x}; z) = \rho_0 \ln[(2h - z)/(2h + z)]$ and thus $E(\boldsymbol{k}) = 2h \tanh[1/(\rho_0 t(\boldsymbol{k})]$.

B. Higgs transition ($K \gg w$)

According to the Feynman rules, fermionic operators are glued together with e particles (i.e., the ends of $W^{(e)}_{\gamma_{r,r'}}$ strings) in the deconfining phase of the toric code. Technically, this is reflected in the Green's function obtained by the resummation of diagrams of type Fig. 4(e):

$$G(\boldsymbol{r}_f, \boldsymbol{r}_i; \tau_f, \tau_i) = \mathbf{D}(\boldsymbol{r}_f, \boldsymbol{r}_i; \tau_f, \tau_i) G_{\text{FS}}(\boldsymbol{r}_f, \boldsymbol{r}_i; \tau_f, \tau_i). \quad (8)$$

When $J \neq 0$, strings $\mathbf{D}(\boldsymbol{r}_f, \boldsymbol{r}_i; \tau_f, \tau_i)$ are nonzero even for $\boldsymbol{r}_f \neq \boldsymbol{r}_i$. They describe the dynamics of e particles and lead to finite $\langle \sigma^z_b(\tau) \sigma^z_{b'}(\tau') \rangle$ correlators. We first concentrate on the OM phase, where the propagator of e particles is determined self-consistently to be

$$\mathbf{D}(\boldsymbol{q}; i\omega) = \frac{4h}{\omega^2 + 4h\{h - 2J[\cos(q_x) + \cos(q_y)]\}}. \quad (9)$$

The inclusion of small nearest-neighbor hopping t leads to the replacement $J \to J + \bar{t}$ in Eq. (9), see Fig. 4(f), where $\bar{t} = 2t G_{\text{FS}}(r + \hat{e}_x, r; \tau, \tau)$. At small J, $\bar{t}$ the intersite Green's function is finite, but exponentially suppressed.

The zero-frequency, zero-momentum correlator $\mathbf{D}(\boldsymbol{q} = 0; i\omega = 0)$ represents the sum over electric strings of any spatiotemporal extent. Its divergence at $4(J + \bar{t}) = h$ signals the confinement-deconfinement quantum phase transition of the toric code [35,41–43]. For even larger $J + \bar{t}$, the condensation of e particles imposes the breakdown of topological order and the propagator is $\mathbf{D}(\boldsymbol{q}; i\omega) = Z(2\pi)^3 \delta(\boldsymbol{q}) \delta(\omega) + \delta \mathbf{D}(\boldsymbol{q}; i\omega)$. According to Eq. (8), fermions form an ordinary Fermi liquid, for which the toric code order parameter $\sqrt{Z}$ determines the fermionic quasiparticle weight.

To determine the behavior near criticality, one has to incorporate renormalization corrections to the strings and
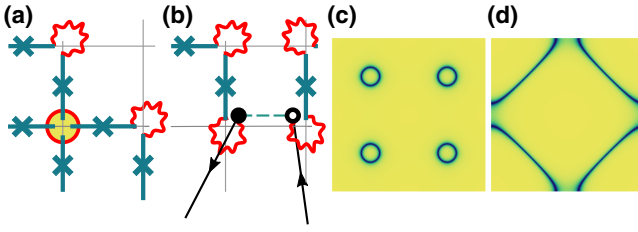
FIG. 5. (a), (b) Interaction of order-parameter field with itself (with fermions) (four-point correlators of e particles are represented as a disk). (c), (d) Spectral weight in the extended Brillouin zone in the confined semimetallic (confined metallic) phase at 10% doping above half filling and elastic scattering rate $1/\tau = 0.2w$.

fermionic propagators in Figs. 4(e) and 4(f). This is most systematically achieved within an effective field theory $S = S_\phi + S_\psi + S_{\text{int}}$ with

$$S_\phi = \int d\tau d^2x \, \frac{1}{2}\phi\big[-\partial_\tau^2 - v^2\nabla^2 + r\big]\phi + \frac{\lambda}{4}\phi^4, \quad (10a)$$

$$S_\psi = \int d\tau d^2x \, \bar{\psi}_\alpha[\partial_\tau + \epsilon_0(-i\partial_x, -i\partial_y)]\psi_\alpha, \quad (10b)$$

$$S_{\text{int}} = \int d\tau d^2x \, g\phi^2\bar{\psi}_\alpha[\cos(-i\partial_x) + \cos(-i\partial_y)]\psi_\alpha. \quad (10c)$$

The neutral field ϕ (ψ) describes the critical fluctuation of strings (of the fermions), $\mathbf{D}(\boldsymbol{x};\tau) = 4ha^2\langle\phi(\boldsymbol{x},\tau)\phi(0,0)\rangle$ ($G_{\text{FS}}(\boldsymbol{x};\tau) = a^2\langle\bar{\psi}(\boldsymbol{x},\tau)\psi(0,0)\rangle$), where a is the lattice constant. We can thus identify $r = 4h(h - 4(J + \bar{t}))$, $v^2 = 4h(J + \bar{t})a^2$. Moreover, we determined the coupling constants $\lambda \sim a^2 J^4/h$ [cf. Fig. 5(a)] and $g \sim a^2 ht$ [cf. Fig. 5(b) and Appendix E, note the form factor in Eq. (10c) due to nearest-neighbor fermionic insertions] and we reiterate that this field theory is designed to incorporate perturbations on top of the integrable theory, hence $g \propto t$. As an important corollary of the microscopic derivation, at $t = 0$ the presence of fermions does not affect the 3D Ising criticality, yet it is a relevant perturbation [33,44,45]. The critical theory Eqs. (10) can then be used to determine a variety of critical properties at the Higgs transition. Most prominently, the quasiparticle weight plays the role of the order parameter, i.e., $Z \sim |h^2 r/J^4|^{2\beta}$ where $\beta \approx 0.33$ [(2 + 1)D Ising].

C. Higgs transition ($K \ll -w$)

We now return to the Higgs transition induced by perturbing the OSM phase with Eq. (6). Conceptually, the same steps which we outlined for the OM hold in the OSM case, too. However, the nontrivial representation of translational symmetry in the flux-phase implies several subtleties [see Appendix E for details, including a derivation of the OSM analog of Eqs. (10)]: (i) The propagator $\mathbf{D}(\boldsymbol{r}_f, \boldsymbol{r}_i; \tau_f, \tau_i)$ is a matrix which acts in the space of the basis of the two-atomic unit cell. (ii) As a consequence, the transition occurs at a slightly higher numerical value of $(J + \bar{t})/h = 1/\sqrt{8}$ and there are two momenta $\boldsymbol{q}$ in the Brillouin zone, at which $\mathbf{D}(\boldsymbol{q}, i\omega = 0)$ diverges. (iii) The relative size of the two order parameter fields near these two momenta defines a 2D vector—hence the Higgs (confinement/deconfinement) transition is in the XY rather than Ising [46] universality class. For any orientation of the 2D
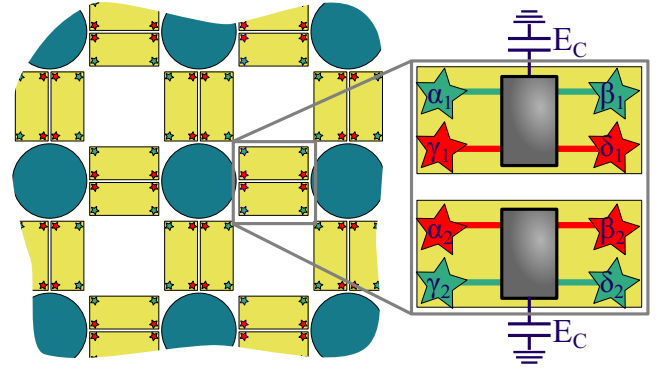
vector, the real-space structure of the Higgs condensate is inhomogeneous. (iv) The critical theory $S_\phi + S_\psi + S_{\text{int}}$ contains a *complex* boson ϕ, two Dirac fermions ψ, and an interaction term S_{int}, which in the XY case, however, is renormalization group irrelevant [47]. (v) According to Eq. (8), the confined phase inherits the small Fermi surfaces of the deconfined OSM phase. By Oshikawa-Luttinger theorem, this is only possible since lattice translational symmetry is spontaneously broken in the confined semimetallic phase. (vi) Nonetheless, the fermionic spectral weight is perfectly translationally invariant, and for comparison to the metal plotted in the large Brillouin zone in Fig. 5(c). (vii) The quasiparticle residue of this spectral weight is momentum independent and appears as $Z \sim |h^2 r/J^4|^{2\beta}$, where $\beta = 0.35$ [(2 + 1)D XY].

IV. IMPLEMENTATION

We conclude by noting that our model can be implemented as a quantum circuit involving interpenetrating lattices of quantum dots and Majorana Cooper pair boxes (MCBs), Fig. 6 (see Appendix F for details). This solid-state proposal complements earlier proposals based on cold-atomic experimental setups [36]. On each MCB island, a large charging energy E_C fixes the charge and thereby encodes a qubit [48,49], where the two degenerate quantum states, $|\downarrow\rangle$ ($|\uparrow\rangle$), have N_0 ($N_0 - 2$) particles in the condensate and empty (filled) pairs of Majorana modes. It has been proposed [50,51] that virtual hopping couples arrays of qubits to develop plaquette and star terms of the toric code.

The interpenetrating array of quantum dots (represented as blue discs in Fig. 6) contains one spinless electron per site and materializes the lattice sites [circles in Fig. 1(a)]. The logical qubits [squares in Fig. 1] are encoded in a pair of adjacent MCBs, in which easy-axis Ising superexchange selects a ground-state Hilbert space spanned by $|\uparrow_1, \downarrow_2\rangle, |\downarrow_1, \uparrow_2\rangle$.

FIG. 6. A quantum emulator of Eqs. (1) is composed of an array of pairs of Majorana Cooper pair boxes (MCBs) (yellow rectangles in which Majorana modes are represented as stars), which encode the qubits on the links of Fig. 1(a) and quantum dots (blue disks), which host the conduction electrons on the sites of Fig. 1(a). Inset: Each MCB consists of two Kitaev chains which are coupled to a floating mesoscopic superconductor and capacitively coupled to the ground. If one out of two MCBs has occupied Majorana modes, a single charge can virtually hop from $\gamma_1 \to \alpha_2$ and back from $\beta_2 \to \delta_1$, which lowers the energy (antiferromagnetic Ising superexchange).

Virtual cyclic exchange of Majorana fermions around an empty plaquette generates H_K in Eqs. (1), which due to the spatial separation of internal (red) and external (green) Marojana modes is unaffected by the quantum dots. Similarly, the star term derives from cyclic exchange of Majorana fermions around a quantum dot. Under appropriate tuning of microscopic parameters, it picks up an additional phase π when the dot is occupied by electrons [i.e., H_h in Eqs. (1)]. Finally, electron hopping between quantum dots occurs via a two-step virtual process, hybridizing with the Majoranas at the red sites to produce the spin-dependent hopping term of strength w in Eqs. (1). Experimental signatures of fermions in these artificial $\mathbb{Z}_2$ gauge theories, e.g., fermionic correlators, can be readily accessed by electronic coupling to the quantum dots. We leave details of this and similar implementations, in particular, the study of additional integrability breaking terms and experimental signatures, to future studies [52].

V. SUMMARY

In summary, inspired by parallels between quantum information theory and correlated electron systems, by coupling Kitaev's toric code to mobile fermions we have obtained a simple, solvable model for fermions in the deconfined phase of a $\mathbb{Z}_2$ gauge theory which can be simulated in an analog quantum computer. The phase diagram of this model contains a transition with abrupt changes in the Fermi surface topology between an OM and OSM through a sequence of symmetry-breaking states. We have further been able to characterize the Higgs transition away from the integrable point using diagrammatic perturbation theory and leave the quantum phase transitions between (orthogonal) semimetallic and metallic states at finite J/h (blurry line in Fig. 1) to future studies.

Although our model is too abstract for direct application to real materials, there are a number of interesting observations that may be of experimental relevance. For example, in our model the small Fermi-surface phase displays parallels with the phenomenology of the pseudogap phase in the cuprates [53]. In light of such resemblances, we believe that the strategy of this work, i.e., condensing crucial emergent physical characteristics of quantum materials and analyzing them in a quantum information setting, will be a valuable scientific method for future research.

APPENDIX A: RELATIONSHIP TO FERMION-ISING-HIGGS GAUGE THEORY

In this Appendix, we explicitly relate the model of Gazit *et al.* [23] to the fermionic toric code. We generalize the steps presented in Ref. [54].

1. Fermion-Ising-Higgs gauge theory

The model of Ref. [23] contains $\bar{\sigma}_b^{x,y,z}$ Pauli matrices describing a $\mathbb{Z}_2$ gauge field which lives on the bonds $\boldsymbol{b}$ of a square lattice. It also contains $\tau_r^{x,y,z}$ Pauli matrices describing Higgs matter (slave spins) on the vertices $\boldsymbol{r}$ of the same lattice and spinful fermions $f_{\boldsymbol{r},\alpha}$ living also on the vertices. The Hamiltonian is

$$\mathcal{H} = \mathcal{H}_{\mathbb{Z}_2} + \mathcal{H}_\tau + \mathcal{H}_f + \mathcal{H}_c + \mathcal{H}_U, \tag{A1a}$$

where

$$\mathcal{H}_{\mathbb{Z}_2} = -K \sum_\square \prod_{\boldsymbol{b} \in \square} \bar{\sigma}_b^z - g \sum_{\boldsymbol{b}} \bar{\sigma}_b^x, \tag{A1b}$$

$$\mathcal{H}_\tau = -J \sum_{\boldsymbol{b}_{r,r'}} \bar{\sigma}_{\boldsymbol{b}_{r,r'}}^z \tau_{\boldsymbol{r}}^z \tau_{\boldsymbol{r'}}^z - h \sum_{\boldsymbol{r}} \tau_{\boldsymbol{r}}^x, \tag{A1c}$$

$$\mathcal{H}_f = -w \sum_{\boldsymbol{b}_{r,r'}} \bar{\sigma}_{\boldsymbol{b}_{r,r'}}^z f_{\boldsymbol{r},\alpha}^\dagger f_{\boldsymbol{r'},\alpha}, \tag{A1d}$$

$$\mathcal{H}_c = -t \sum_{\boldsymbol{b}_{r,r'}} \tau_{\boldsymbol{r}}^z f_{\boldsymbol{r},\alpha}^\dagger \tau_{\boldsymbol{r'}}^z f_{\boldsymbol{r'},\alpha}, \tag{A1e}$$

$$\mathcal{H}_U = U \sum_{\boldsymbol{r}} (\hat{n}_{\boldsymbol{r},\uparrow} - 1/2)(\hat{n}_{\boldsymbol{r},\downarrow} - 1/2). \tag{A1f}$$

The symmetries of this Hamiltonian are [23]:
(i) global SU(2) (spin): $f_{\boldsymbol{r},\alpha} \to U_{\alpha\beta} f_{\boldsymbol{r},\beta}$,
(ii) at $\mu = 0$: global isospin SU(2) in particle-hole space, and
(iii) local $\mathbb{Z}_2$ generated by the conserved charges $\bar{Q}_{\boldsymbol{r}} = \underbrace{(-1)^{\hat{n}_r} \tau_{\boldsymbol{r}}^x}_{\text{matter}} \underbrace{\prod_{\boldsymbol{b} \in +_r} \bar{\sigma}_b^x}_{\text{gauge field}}$, where $\hat{n}_{\boldsymbol{r}} = f_{\boldsymbol{r},\alpha}^\dagger f_{\boldsymbol{r},\alpha}$.

We highlight that part of this Hamiltonian, $\mathcal{H}_{\mathbb{Z}_2} + \mathcal{H}_f$ was studied before, e.g., in Refs. [19,33].

2. Physical origin within $\mathbb{Z}_2$ slave-spin theories

We briefly comment on the connection between this model and $\mathbb{Z}_2$ slave-spin theory as introduced by Rüegg *et al.* [11].

Consider a model of spinful fermions on a square lattice:

$$\mathcal{H}_{\text{Hubbard}+\ldots} = -t_0 \sum_{\boldsymbol{b}_{r,r'}} c_{\boldsymbol{r},\alpha}^\dagger c_{\boldsymbol{r'},\alpha}$$
$$+ \sum_{\boldsymbol{r}} [U_0 \hat{n}_{\boldsymbol{r}}(\hat{n}_{\boldsymbol{r}} - 1) - \mu \hat{n}_{\boldsymbol{r}}] + \ldots. \tag{A2}$$

The terms "..." represent additional nonlocal terms which are not further specified (see discussion below). In the case when the Hubbard U_0 is twice the chemical potential, the on-site problem contains two twofold degenerate levels. These may be represented by a spin variable, using $\langle \tau_{\boldsymbol{r}}^x \rangle = 1$ ($\langle \tau_{\boldsymbol{r}}^x \rangle = -1$) for the singly occupied states at energy $-\mu$ (empty or doubly occupied states at energy 0). In the slave-spin formulation, we have thus fractionalized the conduction electrons:

$$c_{\boldsymbol{r}}^\dagger = f_{\boldsymbol{r}}^\dagger \tau_{\boldsymbol{r}}^z. \tag{A3}$$

In this representation,

$$\mathcal{H}_{\text{Hubbard}+\ldots} = -t_0 \sum_{\boldsymbol{b}_{r,r'}} f_{\boldsymbol{r},\alpha}^\dagger \tau_{\boldsymbol{r}}^z f_{\boldsymbol{r'},\alpha} \tau_{\boldsymbol{r'}}^z - U_0 \sum_{\boldsymbol{r}} \tau_x + \ldots, \tag{A4}$$

using the on-site constraint $(-1)^{\hat{n}_{\boldsymbol{r}}} \tau_{\boldsymbol{r}}^x = 1$.

Depending on the nature of the additional unspecified terms denoted . . . in the previous equation, a series of renormalization group steps may then lead to Eqs. (A1) as an effective low-energy theory (with the more general gauge invariant constraint $\bar{Q}_r = 1$). By reversing the arguments, the physics discussed in this paper is applicable for those models which are in the basin of attraction of the fix-point Hamiltonian Eqs. (A1). In particular, note that h in Eqs. (A1) corresponds to the on-site repulsion of the extended Hubbard model Eq. (A2).

3. Formulation in terms of gauge invariant quantities

Since the total, local charge is conserved, we can impose Gauss's law on the physical Hilbert space:

$$\bar{Q}_r |\text{Phys}\rangle = |\text{Phys}\rangle \quad \text{(Gauss's law).} \quad \text{(A5)}$$

We readily see that gauge invariant quantities are

(1) c electrons: $c_{r,\alpha} = \tau_r^z f_{r,\alpha}$.

(2) $\mathbb{Z}_2$ electric strings along a contour $\gamma_{r,r'}$ between r, r': $W_{\gamma_{r,r'}}^{(e)} = \tau_r^z [\prod_{b \in \gamma_{r,r'}} \bar{\sigma}_b^z] \tau_{r'}^z \equiv \prod_{b \in \gamma_{r,r'}} \sigma_b^z$.

(3) Of course, $\bar{\sigma}_b^x \equiv \sigma_b^x$ (magnetic strings) and $\hat{n}_r = f_{r,\alpha}^\dagger f_{r,\alpha} = c_{r,\alpha}^\dagger c_{r,\alpha}$ are trivially gauge invariant.

Here we have introduced Pauli matrices without a bar, $\sigma_b^z = \prod_{r \in \partial b} \tau_r^z \bar{\sigma}_b^z$ and $\sigma_b^x = \bar{\sigma}_b^x$, which clearly also have the appropriate commutation relations. Except [54] for special lines $J = 0$ or $g = 0$, all states of $\mathcal{H}_{\mathbb{Z}_2} + \mathcal{H}_\tau$ can be fully specified in the unitary gauge in which $\tau_r^z |\text{phys}\rangle = |\text{phys}\rangle$. (Indeed, within the physical subspace, where $\tau_r^x \to (-1)^{\hat{n}_r} \prod_{b \in +_r} \sigma_b^x$, the Hamiltonian $\mathcal{H}$ preserves this gauge choice.) In short, having fixed the gauge $Q_r |\text{phys}\rangle = |\text{phys}\rangle = \tau_r^z |\text{phys}\rangle$ allows us to express all gauge-invariant quantities without resorting to τ operators,

$$\mathcal{H} = \mathcal{H}_{\mathbb{Z}_2} + \mathcal{H}_\tau + \mathcal{H}_f + \mathcal{H}_c + \mathcal{H}_U, \quad \text{(A6a)}$$

where

$$\mathcal{H}_{\mathbb{Z}_2} = -K \sum_\square \prod_{b \in \square} \sigma_b^z - g \sum_b \sigma_b^x, \quad \text{(A6b)}$$

$$\mathcal{H}_\tau = -J \sum_b \sigma_b^z - h \sum_r \prod_{b \in +_r} (-1)^{\hat{n}_r} \sigma_b^x, \quad \text{(A6c)}$$

$$\mathcal{H}_f = -w \sum_{b_{r,r'}} \sigma_{b_{r,r'}}^z c_{r,\alpha}^\dagger c_{r',\alpha}, \quad \text{(A6d)}$$

$$\mathcal{H}_c = -t \sum_{b_{r,r'}} c_{r,\alpha}^\dagger c_{r',\alpha}, \quad \text{(A6e)}$$

$$\mathcal{H}_U = U \sum_r (\hat{n}_{r,\uparrow} - 1/2)(\hat{n}_{r,\downarrow} - 1/2). \quad \text{(A6f)}$$

This is a fermionic toric code, and at $g = J = t = U = 0$ the same as Eqs. (1) of the main text.

APPENDIX B: SYMMETRIES IN THE ORTHOGONAL SEMIMETAL PHASE

1. Explicit construction of the π-flux states

Here, we solve the π-flux model in the gauge where $\langle \sigma_b^z \rangle = (-1)^{b_x}$, i.e., it is negative on every other vertical column but positive everywhere else (see Fig. 7). We choose a two-
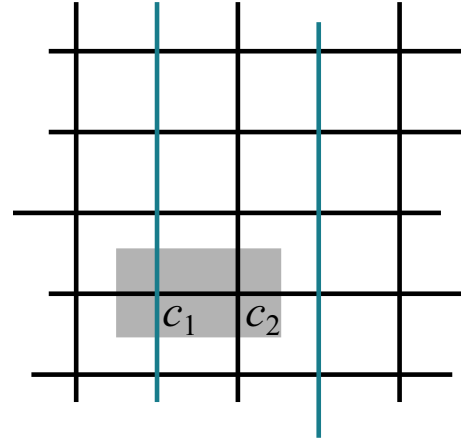

FIG. 7. Unit cell (shaded gray) and flux configuration prior to application of Q_r operators in the OSM phase (green lines represent bonds with $\langle \pi | \sigma_b^z | \pi \rangle = -1$).

atom unit cell of dimers along the x direction and Fourier transform,

$$c_{x,1} = \int_{\text{small BZ}} (dk) e^{ikr} c_{k,1}, \quad \text{(B1)}$$

$$c_{x,2} = \int_{\text{small BZ}} (dk) e^{ikr + ik_x x} c_{k,2}. \quad \text{(B2)}$$

(Note that 1,2 labels do not correspond to sublattice labels A, B). The momentum space Hamiltonian is

$$H = -2w \int_{\text{small BZ}} (dk) c_k^\dagger [-\cos(k_y)\gamma_z + \cos(k_x)\gamma_x] c_k \quad \text{(B3)}$$

[the small Brillouin zone (BZ) is $k \in (-\pi/2, \pi/2) \times (-\pi, \pi)$], which implies a dispersion

$$\epsilon_\pi^{(\pm)}(k) = \pm 2w \sqrt{\cos(k_x)^2 + \cos(k_y)^2}. \quad \text{(B4)}$$

Dirac nodes occur at $|k_x| = |k_y| = \pi/2$.

2. Projective representation of translational symmetry

In this Appendix section, we explicitly demonstrate the projective representation of translational symmetry. For simplicity, we consider a system below half filling. For the gauge choice $|\pi\rangle_\sigma$ discussed above, $\langle \pi | \sigma_b^z | \pi \rangle_\sigma = (-1)^{b_x}$, the Fermi surface is given by

$$|\text{FS}\rangle_c = \prod_{k \in \text{FS}} (c_{k,1}^\dagger, c_{k,2}^\dagger) \psi_k^{(-)} |0\rangle$$

$$= \prod_{k \in \text{FS}} \sum_{x,x'} e^{ik(x-x')} (c_{x,1}^\dagger, c_{x,2}^\dagger) \psi_{x'}^{(-)} |0\rangle, \quad \text{(B5)}$$

where $\psi_k^{(-)}$ is the two-component eigenstate of $h(k) = -\cos(k_y)\gamma_z + \cos(k_x)\gamma_x$ with energy $\epsilon_\pi^{(-)}(k)$.

We now consider a different gauge choice, $|\pi'\rangle_\sigma$, in which the columns of minus signs have been shifted by one lattice constant, $\langle \pi' | \sigma_b^z | \pi' \rangle_\sigma = (-1)^{b_x+1}$. It has a different Slater wave function, i.e.,

$$|\text{FS}'\rangle_c = \prod_{k \in \text{FS}} (c_{k,1}^\dagger, c_{k,2}^\dagger) \tilde{\psi}_k^{(-)} |0\rangle$$

$$= \prod_{k \in \text{FS}} \sum_{x,x'} e^{ik(x-x')} (c_{x,1}^\dagger, c_{x,2}^\dagger) \tilde{\psi}_{x'}^{(-)} |0\rangle. \quad \text{(B6)}$$
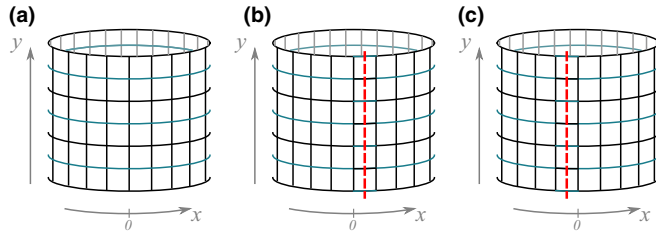
FIG. 8. Flux insertion argument in the OSM phase. (a) Representation of $|\pi\rangle_\sigma$ (analogous to Fig. 7) prior to the insertion of a π flux. (b) Configuration $|\pi\rangle_\sigma$ after insertion of a π flux. (c) Translation of the latter $|\pi\rangle_\sigma$.

Since $|\pi'\rangle_\sigma$ induces a fermionic hopping Hamiltonian $\tilde{h}(\boldsymbol{p}) = h(p_x, p_y + \pi)$, it follows that $\tilde{\psi}_{\boldsymbol{k}}^{(-)} = \psi_{k_x, k_y+\pi}^{(-)}$.

We now demonstrate that $|\pi'\rangle_\sigma |\text{FS}'\rangle_c = \prod_{\boldsymbol{r}\in(\mathbb{Z},2\mathbb{Z})} Q_{\boldsymbol{r}} |\pi\rangle_\sigma |\text{FS}\rangle_c$ and hence $\prod_{\boldsymbol{r}} \hat{P}_{\boldsymbol{r}} |\pi'\rangle_\sigma |\text{FS}'\rangle_c = \prod_{\boldsymbol{r}} \hat{P}_{\boldsymbol{r}} |\pi\rangle_\sigma |\text{FS}\rangle_c$ (i.e., the two seemingly different states Eqs. (B5) and (B6) are the same in the deconfined phase: translational symmetry is restored). It is easy to see that the string of $Q_{\boldsymbol{r}}$ operators translates the columnar gauge field pattern of negative bonds by one. The effect of the fermionic parity operator requires a little more explanation:

$$\prod_{\boldsymbol{r}\in(\mathbb{Z},2\mathbb{Z})} (-1)^{\hat{n}_{\boldsymbol{r}}} |\text{FS}'\rangle_c$$

$$= \prod_{\boldsymbol{k}\in\text{FS}} \sum_{\boldsymbol{x},\boldsymbol{x}'} e^{i\boldsymbol{k}(\boldsymbol{x}-\boldsymbol{x}')}(-1)^y (c_{\boldsymbol{x},1}^\dagger, c_{\boldsymbol{x},2}^\dagger)\tilde{\psi}_{\boldsymbol{x}'}^{(-)} |0\rangle$$

$$= \prod_{\boldsymbol{k}\in\text{FS}} (c_{\boldsymbol{k},1}^\dagger, c_{\boldsymbol{k},2}^\dagger)\tilde{\psi}_{(k_x,k_y+\pi)}^{(-)} |0\rangle$$

$$= |\text{FS}\rangle_c . \quad (B7)$$

In the second line, we have used that the spectrum (and thus the Fermi surface) is invariant under shifts of π in the y direction.

APPENDIX C: LUTTINGER'S THEOREM

In this Appendix, we explain why the vanishing Fermi surface in the OSM at half filling is consistent with the Oshikawa-Luttinger-theorem [14]. We follow arguments similar to those presented by Paramekanti and Vishwanath [16].

To this end, we consider a our model, Eqs. (1), on a finite cylinder as in Fig. 8.

We first remind the reader about the Oshikawa-Luttinger theorem for conventional Fermi liquids. We summarize the main physics and leave mathematical and technical details to the original literature. After the adiabatic insertion of a flux 2π through the hole of the cylinder, the many-body Hamiltonian is gauge equivalent to the Hamiltonian prior to the insertion of the flux. Thus all eigenstates are the same. Still, by simple electrodynamics, the cylinder now spins due to the electromotive force and the total (angular) momentum of the system is $\Delta P_x = 2\pi L_y n$ (where n is the average particle number per site). In a Fermi liquid, the quasiparticles excitation near the Fermi surface acquire a momentum because the Fermi distribution is shifted in the x direction. A simple integration by parts yields $\Delta P_x^{\text{FS}} = L_y V_{\text{FS}}/2\pi$, where V_{FS} is
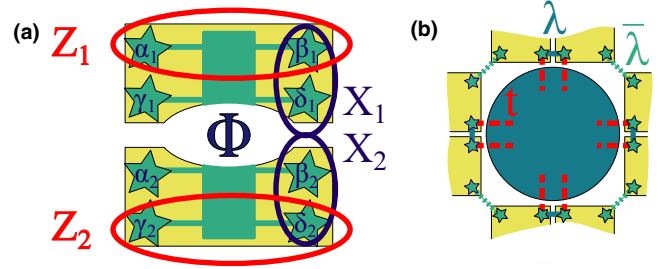

FIG. 9. Details on the quantum emulator presented in Fig. 6 of the main text. (a) Each block emulating the toric code degrees of freedom consists of two MCBs which are threaded by a flux. When E_C is the largest scale, each MCB is a two-level system in which Z and X gates (Pauli matrices) can be defined as bilinears of Majoranas, see Eq. (F1). Virtual superexchange induces a pseudomagnetic Ising coupling between adjacent MCBs. Note that our convention of labeling Majoranas in vertical boxes is the counterclockwise 90° rotation of panel (a), whence Z gates are always along the elongated sides of the rectangle. (b) The Majorana modes and the fermions on the quantum dot are coupled by hopping matrix elements of amplitude $\lambda, \bar{\lambda}, t$.

the volume enclosed by the Fermi surface. In a Fermi liquid, the only momentum carrying particles are the quasiparticles and therefore $\Delta P_x = \Delta P_x^{\text{FS}} \pmod{2\pi L_y}$ and thus

$$\frac{V_{\text{FS}}}{4\pi^2} = n \pmod 1, \quad (C1)$$

where the addition mod 1 formally stems from crystalline momentum-conservation modulo reciprocal lattice vectors and physically accounts for fully filled bands.

We consider a slightly different setup in the OSM phase. For the state $|\pi\rangle_\sigma$, we consider a gauge choice of the negative bonds as depicted in Fig. 8(a) and thread a flux π through the whole of the cylinder. This flux π in the physical $U(1)$ field can be absorbed into a reconfiguration of σ spins, Fig. 8(b). Despite having inserted only half a flux, it is thus evident that the Hamiltonian after flux insertion H_π is related to H_0 of Eqs. (1) by a simple unitary transformation,

$$H_\pi = W^{(m)} H_0 W^{(m)}, \quad (C2)$$

where $W^{(m)} = \prod_{\boldsymbol{b}\in\mathcal{C}} \sigma_{\boldsymbol{b}}^x$ is given by the magnetic string along the dashed contour presented in Fig. 8(b). Obviously, H_π and H_0 have the same spectrum, and the ground state has evolved from $|\text{GS}_\pi\rangle$ to $W^{(m)} |\text{GS}_\pi\rangle$.

We now demonstrate that, under the assumption $h > 0$ and at half filling, $W^{(m)} |\text{GS}_\pi\rangle$ carries the momentum transferred to the cylinder and at the same time the fermionic distribution function is unaffected. Thus, the momentum balance is accounted for by the deconfining gauge sector. Indeed, we can exploit that translation by one lattice site in the x direction can be equivalent to application of $\prod_{\boldsymbol{r}=(0,y)} \prod_{\boldsymbol{b}\in+_{\boldsymbol{r}}} \sigma_{\boldsymbol{b}}^x = \prod_{\boldsymbol{r}=(0,y)} (-1)^{\hat{n}_{\boldsymbol{r}}} Q_{\boldsymbol{r}}$ which acts solely on the gauge sector and leaves the fermions invariant. We can then use

$$\prod_{\boldsymbol{r}=(0,y)} (-1)^{\hat{n}_{\boldsymbol{r}}} Q_{\boldsymbol{r}} W^{(m)} |\text{GS}_\pi\rangle = e^{i\pi L_y \langle\hat{n}_{\boldsymbol{r}}\rangle} W^{(m)} |\text{GS}_\pi\rangle . \quad (C3)$$

Here, we used that $[Q_{\boldsymbol{r}}, W^{(m)}] = 0$, $Q_{\boldsymbol{r}} |\text{GS}_\pi\rangle = |\text{GS}_\pi\rangle$ and a homogeneous density. At half filling, the momentum balance
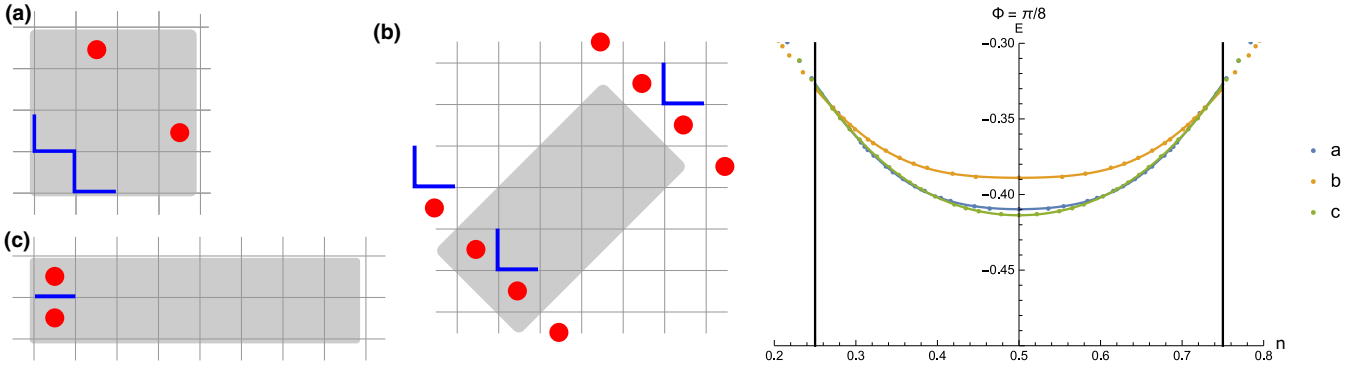
FIG. 10. Configurations of average flux $\Phi = \pi/8$ and associated fermionic ground-state energies as a function of filling.

between $\Delta P_x = \pi L_y n$ (from electrodynamics) and $\Delta P_x^{|\pi\rangle_\sigma} = \pi L_y \langle \hat{n}_r \rangle$ trivially reproduces $n = \langle \hat{n}_r \rangle$ (valid only at half filling $n = 1/2$) without resorting to the Fermi surface.

We now relax one of the two assumptions outlined above and consider a filling away from 1/2. Then, in the OSM phase, the Luttinger-Oshikawa theorem implies a balance which is shifted by 1/2 as compared to Eq. (C1):

$$\frac{V_{\text{FS}}}{4\pi^2} + \frac{1}{2} = n \pmod 1. \tag{C4}$$

Finally, we relax the second assumption for the derivation of the modified Luttinger theorem and comment on the case in which $h < 0$ in which the ground state obeys $Q_r |\text{GS}_{0/\pi}\rangle = -|\text{GS}_{0/\pi}\rangle$. [Clearly, one may construct ground states for this case analogous to Eqs. (2) in the main text.] For spinless fermions, the model Eqs. (1) at negative h is related to the same model at positive h by a particle-hole transformation $c_r \leftrightarrow c_r^\dagger$; $\sigma_b^{x,z} \to -\sigma_b^{x,z}$. Therefore, all the conclusions obtained for Eqs. (1) at $h > 0$ are applicable to $h < 0$, as well.

APPENDIX D: DIAGRAMMATIC RULES

In this Appendix, we present the diagrammatic rules for imaginary time-ordered, ground-state correlators of fermionic operators $O_r(\tau) \in \{c_r(\tau), c_r^\dagger(\tau)\}$ and $\sigma_b^z(\tau)$ insertions

$$C(\{r; b; \tau\}) = -\langle \text{GS}|\mathcal{T}\left[\prod_n O_{r_n}(\tau_n) \prod_m \sigma_{b_m}^z(\tau_m)\right]|\text{GS}\rangle. \tag{D1}$$

(1) Draw $\circ$ for $c_r(\tau)$, $\bullet$ for $c_r^\dagger(\tau)$, $\times$ for $\sigma_b^z(\tau)$ at the corresponding position r, b in real space.

(2) Only configurations with an even number of operators per site can be nonzero, $N_\circ + N_\bullet + N_\times \in 2\mathbb{N}_0$ (gauge-field operators σ_b^z are associated to both adjacent sites $r \in \partial b$).

(3) Connect operators associated to a given site as follows:

(a) For two operators at times τ_1, τ_2, draw a wavy line which means $D(\tau_1, \tau_2) = e^{-2h|\tau_1 - \tau_2|}$.

(b) For $2l > 2$ operators at times τ_m ($m \in \{1, \ldots 2l\}$), encircle the operators which means $e^{-2h\sum_{k=1}^{2l}(-1)^k(\mathcal{T}\{\tau_m\})_k}$, where $\mathcal{T}$ time orders the string of times $\{\tau_m\}$ in ascending order.

(4) Evaluate all $\times$ by $\langle 0|\sigma_b^z|0\rangle_\sigma$ ($\langle \pi|\sigma_b^z|\pi\rangle_\sigma$) in the OM (OSM) phase.

(5) Connect all $\circ$ and $\bullet$ in all possible combinations according to the standard rules for fermionic diagrammatics with solid lines representing the ordinary Green's function $G_{\text{FS}}(r_1, r_2; \tau_1, \tau_2) = -\langle \text{FS}_{0/\pi}|\mathcal{T}[c_{r_1}(\tau_1)c_{r_2}^\dagger(\tau_2)]|\text{FS}_{0/\pi}\rangle$.

Derivation of these rules.

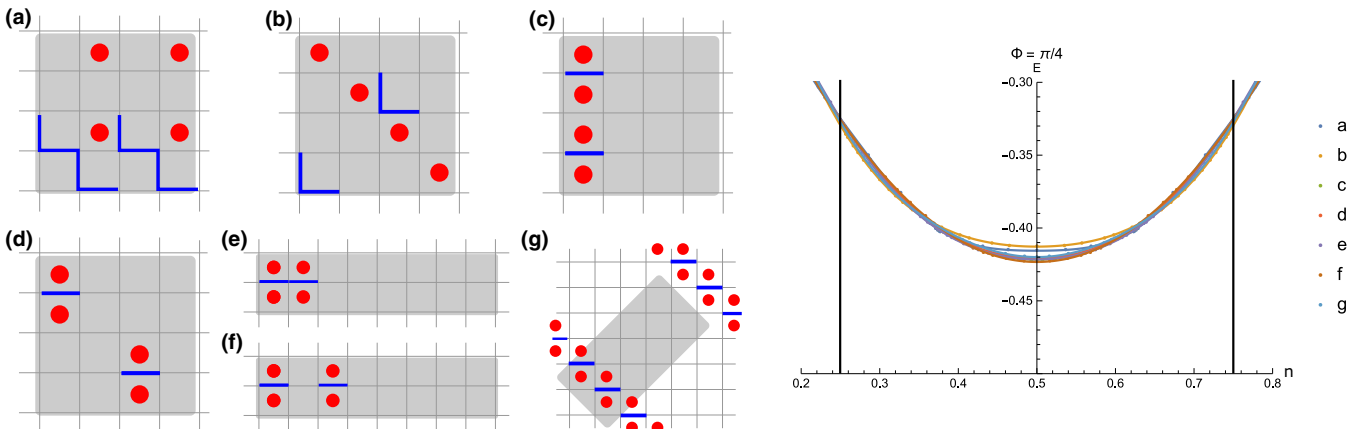FIG. 11. Configurations of average flux $\Phi = \pi/4$ and associated fermionic ground-state energies as a function of filling.

(1) We use $|GS\rangle = \prod_{\boldsymbol{r}} \hat{P}_{\boldsymbol{r}} |FS\rangle_c |0/\pi\rangle_{\sigma}$, and pass the projectors over the string of operators to find that $\langle GS| \mathcal{T}[O_{\boldsymbol{r}_n}(\tau_n) \dots O_{\boldsymbol{r}_1}(\tau_1) \sigma^z_{\boldsymbol{b}'_m}(\tau'_m) \dots \sigma^z_{\boldsymbol{b}'_1}(\tau'_1)]|GS\rangle$ vanishes, unless an even number of operators is associated to each site (each $\sigma^z_{\boldsymbol{b}}$ is associated to both adjacent sites $\boldsymbol{r} \in \partial\boldsymbol{b}$). Therefore,

(a) all fermionic operators are connected by "electric" strings of σ^z (includes the possibility of two fermions on the same position, i.e., strings of zero extension);

(b) all electric strings are either closed or end in fermionic operators.

[We used $\hat{P}_{\boldsymbol{r}} = [1 + Q_{\boldsymbol{r}}]/2$ and we will repeatedly use $Q_{\boldsymbol{r}} O_{\boldsymbol{r}'} = (-1)^{\delta_{\boldsymbol{r},\boldsymbol{r}'}} O_{\boldsymbol{r}'} Q_{\boldsymbol{r}}$ and $Q_{\boldsymbol{r}} \sigma^z_{\boldsymbol{b}} = (-1)^{\delta_{\boldsymbol{r}\in\partial\boldsymbol{b}}} \sigma^z_{\boldsymbol{b}} Q_{\boldsymbol{r}}$.]

(2) The interaction picture representation of the fermionic operators $O_{\boldsymbol{r}} \in \{c_{\boldsymbol{r}}, c^{\dagger}_{\boldsymbol{r}}\}$ is $O_{\boldsymbol{r}}(\tau) = e^{H_0\tau} O_{\boldsymbol{r}} e^{-H_0\tau} = \bar{O}_{\boldsymbol{r}}(\tau) e^{2hQ_{\boldsymbol{r}}\tau}$, where $\bar{O}(\tau) = e^{H_c\tau} O_{\boldsymbol{r}} e^{-H_c\tau}$. Similarly, the interaction picture representation of $\sigma^z_{\boldsymbol{b}}(\tau) = \sigma^z_{\boldsymbol{b}} e^{2h\sum_{\boldsymbol{r}\in\partial\boldsymbol{b}} Q_{\boldsymbol{r}}\tau}$.

(3) We (i) explicitly time order the string of operators in $C(\{\boldsymbol{r}, \tau\})$, (ii) use the representation $O_{\boldsymbol{r}}(\tau) = \bar{O}_{\boldsymbol{r}}(\tau) e^{2hQ_{\boldsymbol{r}}\tau}$, $\sigma^z_{\boldsymbol{b}}(\tau) = \sigma^z_{\boldsymbol{b}} e^{2h\sum_{\boldsymbol{r}\in\partial\boldsymbol{b}} Q_{\boldsymbol{r}}\tau}$ that we just derived, (iii) then pass all $e^{2hQ_{\boldsymbol{r}}\tau}$ to the right of all $\bar{O}_{\boldsymbol{r}}(\tau)$, $\sigma^z_{\boldsymbol{b}}$ using again $Q_{\boldsymbol{r}} \bar{O}_{\boldsymbol{r}'}(\tau) = (-1)^{\delta_{\boldsymbol{r},\boldsymbol{r}'}} \bar{O}_{\boldsymbol{r}'}(\tau) Q_{\boldsymbol{r}}$, $Q_{\boldsymbol{r}} \sigma^z_{\boldsymbol{b}} = (-1)^{\delta_{\boldsymbol{r}\in\partial\boldsymbol{b}}} \sigma^z_{\boldsymbol{b}} Q_{\boldsymbol{r}}$, and (iv) finally, use $Q_{\boldsymbol{r}} |GS\rangle = |GS\rangle$ to obtain Feynman rule No. 3 (e.g., exponentials of the kind $e^{-2h|\tau-\tau'|}$ represented by wavy lines).

(4) At this point, the correlator has been evaluated to be $C(\{\boldsymbol{r}, \tau\}) = -\langle GS| \mathcal{T}[\bar{O}_{\boldsymbol{r}_n}(\tau_n) \dots \bar{O}_{\boldsymbol{r}_1}(\tau_1) \sigma^z_{\boldsymbol{b}_m} \dots \sigma^z_{\boldsymbol{b}_1}]|GS\rangle \times$ (*exponentials represented by wavy lines*). The only gauge field (= spin σ) dependence in the operators is now inside H_c entering $\bar{O}(\tau)$ and in the strings of σ^z. We can thus replace all gauge fields by the ground state (e.g., all up in zero flux) configuration $\sigma^z \to \langle\sigma^z\rangle_{|0\rangle/|\pi\rangle}$, $H_c \to H_{0/\pi}$

(5) We have brought the correlator to the form $C(\{\boldsymbol{r}, \tau\}) = -\langle FS| \mathcal{T}[\bar{O}_{\boldsymbol{r}_n}(\tau_n) \dots \bar{O}_{\boldsymbol{r}_1}(\tau_1)]|FS\rangle \times$ (*exponentials represented by wavy lines*). Now we can use the standard Wick's theorem for fermions, this is Feynman rule No. 4.

Analogous rules hold upon Wick-rotation to real time $\tau \to it$, $|\tau_1 - \tau_2| \to i|t_1 - t_2|$.

APPENDIX E: HIGGS TRANSITION

In this Appendix, we present details on the transition from deconfined to confined phases and a derivation of the effective field theory.

1. Zero-flux case (starting point: orthogonal metal)

a. Propagator of e particles

The propagator of $\mathbf{D}(\boldsymbol{r}_f, \boldsymbol{r}_i; \tau_f, \tau_i)$ entering Eq. (8) of the main text is defined according to diagram Fig. 4(e) by

$$\mathbf{D}(\boldsymbol{r}_f, \boldsymbol{r}_i; \tau_f, \tau_i) = D(\tau_f, \tau_i)\delta_{\boldsymbol{r}_f, \boldsymbol{r}_i} + J \int d\tau D(\tau_f, \tau) D(\tau, \tau_i)\delta_{<\boldsymbol{r}_f, \boldsymbol{r}_i>}$$

$$+ J^2 \sum_{\substack{\boldsymbol{b}, \boldsymbol{b}' \text{s.th.} \\ \boldsymbol{r}_f \in \partial\boldsymbol{b}, \boldsymbol{r}_i \in \partial\boldsymbol{b}'}} \int d\tau d\tau' D(\tau_f, \tau) \langle \sigma^z_{\boldsymbol{b}}(\tau) \sigma^z_{\boldsymbol{b}'}(\tau')\rangle D(\tau', \tau_i) [1 - \delta_{<\boldsymbol{r}_f, \boldsymbol{r}_i>} - \delta_{\boldsymbol{r}_f, \boldsymbol{r}_i}].$$

Here, $\delta_{<\boldsymbol{r}_f, \boldsymbol{r}_i>} = 1$ for nearest neighbors, it vanishes otherwise.

The resummation of nonintersecting strings of $\times$ insertions, Fig. 4(e) of the main text, is given by

$$\mathbf{D}(\boldsymbol{r}_f, \boldsymbol{r}_i; i\omega) = D(i\omega)\delta_{\boldsymbol{r}_f, \boldsymbol{r}_i} + J \sum_{\boldsymbol{r}\text{n.N. of }\boldsymbol{r}_f} \langle 0|\sigma^z_{\langle\boldsymbol{r},\boldsymbol{r}_f\rangle}|0\rangle_{\sigma} \mathbf{D}(\boldsymbol{r}, \boldsymbol{r}_i; i\omega)D(i\omega). \tag{E1}$$

In momentum space, this implies $\mathbf{D}(\boldsymbol{q}, i\omega) = D(i\omega) + 2J[\cos(q_x) + \cos(q_y)]D(i\omega)\mathbf{D}(\boldsymbol{q}, i\omega)$ which immediately implies Eq. (9) of the main text. The inclusion of fermionic hopping, see Fig. 3(f), implies $\mathbf{D}_t(\boldsymbol{q}, i\omega) = \mathbf{D}(\boldsymbol{q}, i\omega) + 2\bar{t}[\cos(q_x) + \cos(q_y)]\mathbf{D}(\boldsymbol{q}, i\omega)\mathbf{D}_t(\boldsymbol{q}, i\omega)$ and thus

$$\mathbf{D}_t(\boldsymbol{q}, i\omega) = \frac{4h}{\omega^2 + 4h(h - 2(J + \bar{t})[\cos(q_x) + \cos(q_y)])}. \tag{E2}$$

b. Self-interaction of electric strings

To obtain the mean-field expectation value of Z, we first analyze nonlinearities in $\boldsymbol{D}(\boldsymbol{q}, i\omega)$, which we extract from the connected part of four-point correlation functions.

In the absence of t, the nonlinearity stems from Fig. 5(a) of the main text, i.e.,

$$V(\{\boldsymbol{r}, \tau\}) = J^4 \Big\{ \sum_{\boldsymbol{r}} \prod_{n=1}^{4} \delta_{<\boldsymbol{r}_n, \boldsymbol{r}>}$$

$$\times e^{-2h[(\mathcal{T}\{\tau\})_4 - (\mathcal{T}\{\tau\})_3 + (\mathcal{T}\{\tau\})_2 - (\mathcal{T}\{\tau\})_1]}$$

$$- D(\tau_1, \tau_2)D(\tau_3, \tau_4) - D(\tau_1, \tau_3)D(\tau_2, \tau_4)$$

$$- D(\tau_1, \tau_4)D(\tau_3, \tau_2) \Big\}. \tag{E3}$$

We remind the reader that for more than two wavy lines on a given site, the time dependence of interaction is rather complicated in view of Feynman rule No. 3. Since we only keep the connected part of the four-point correlator, we have subtracted the contributions which correspond to two e-particle propagators running through each other without interaction.
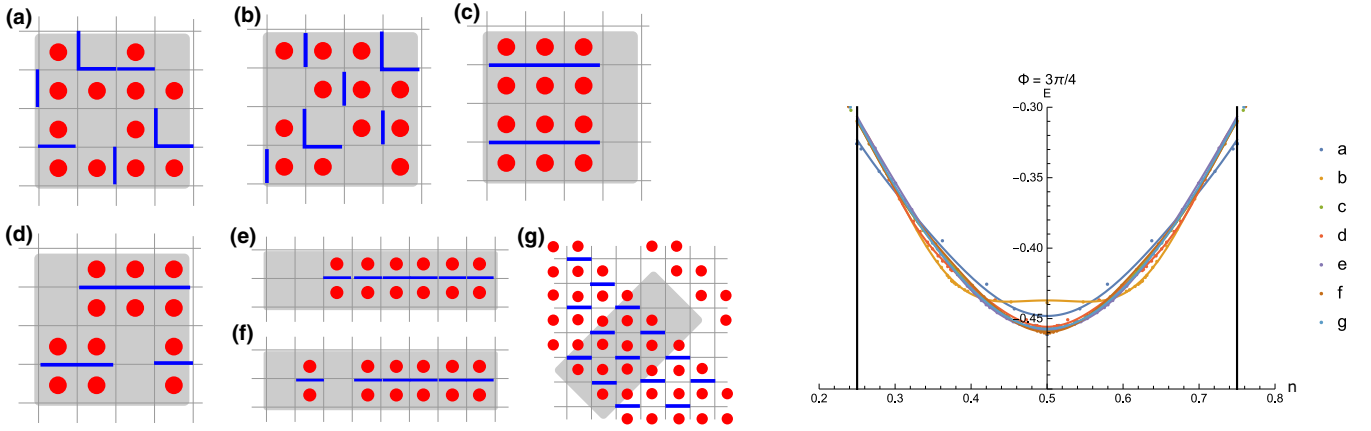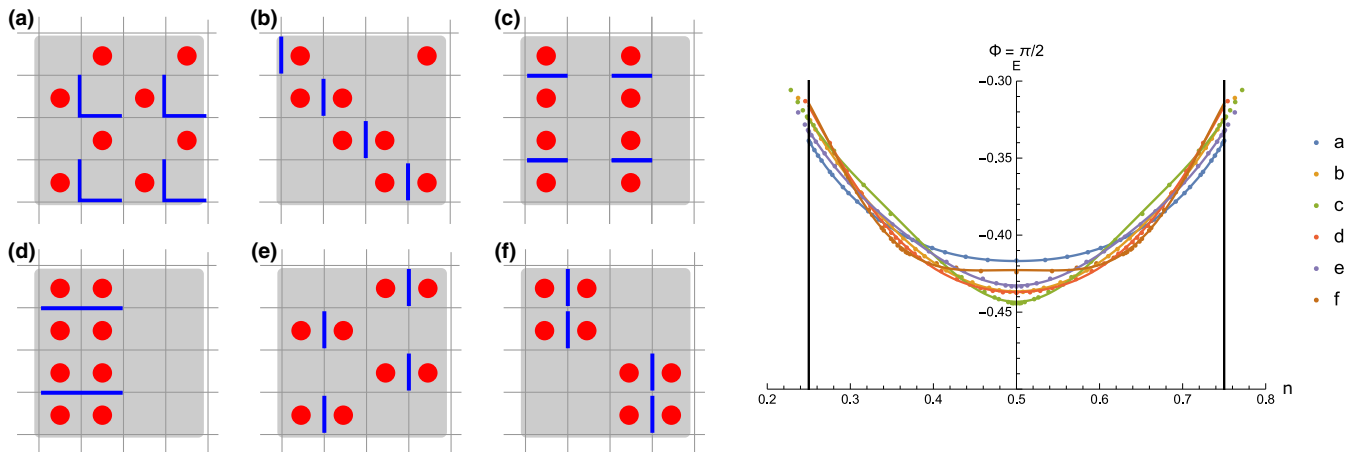
FIG. 12. Configurations of average flux $\Phi = 3\pi/8$ and associated fermionic ground-state energies as a function of filling.

For the derivation of the continuum field theory, we evaluate Eq. (E3) at zero incident frequencies and obtain ($\beta = 1/T$ is the inverse temperatue, viz., the infrared cutoff)

$$\int \prod_n d\tau_n V(\{\boldsymbol{r}, \tau\}) = \left\{ \frac{J^4}{h^2} \left(3\beta^2 - 6\beta/h + 9/(2h^2) \right) \right.$$

$$\left. -3\frac{J^4}{h^2} (\beta - 1/(2h))^2 \right\} \sum_{\boldsymbol{r}} \delta_{<\boldsymbol{r}_n, \boldsymbol{r}>}$$

$$\simeq -J^4 \frac{3\beta}{h^3} \sum_{\boldsymbol{r}} \delta_{<\boldsymbol{r}_n, \boldsymbol{r}>}. \qquad (E4)$$

The bare value of the coeffecent $\lambda \sim a^2 J^4/h$ follows from comparison of Eqs. (E4) and (10) of the main text. We remind the reader that in Eqs. (10), the field ϕ was rescaled by $\sqrt{4ha^2}$ to compensate the numerator of the Green's function and to obtain the continuum limit.

c. Interactions between fermions and strings

In the presence of t perturbations, there are new operator insertions which would imply mutual impact of fermionic excitations and string in Fig. 3(e). The inclusion of nearest-neighbor hopping t yields a local in time interaction:

$$V(\boldsymbol{r}_c, \boldsymbol{r}_{c^\dagger}, \boldsymbol{r}_{D_1}, \boldsymbol{r}_{D_2}) = t \left[\delta_{\boldsymbol{r}_c, \boldsymbol{r}_{D_1}} \delta_{\boldsymbol{r}_{c^\dagger}, \boldsymbol{r}_{D_2}} + 1 \leftrightarrow 2 \right] \delta_{\langle \boldsymbol{r}_c, \boldsymbol{r}_c^\dagger \rangle}. \quad (E5)$$

Upon rescaling of fields (fermions are rescaled by a), this yields a coupling constant $g \sim hta^2(\cos(\hat{p}_x) + \cos(\hat{p}_y))$ in the long-wavelength limit of ϕ fields.

2. π-flux case (starting point: orthogonal semimetal)

a. Propagator of e particles

In the π-flux case the, the resummation

$$\mathbf{D}(\boldsymbol{r}_f, \boldsymbol{r}_i; i\omega) = D(i\omega)\delta_{\boldsymbol{r}_f, \boldsymbol{r}_i} + J \sum_{\substack{\boldsymbol{r} \text{ n.N.} \\ \text{of } \boldsymbol{r}_f}} \left\langle \pi | \sigma^z_{\langle \boldsymbol{r}, \boldsymbol{r}' \rangle} | \pi \right\rangle_\sigma$$

$$\times \mathbf{D}(\boldsymbol{r}, \boldsymbol{r}_i; i\omega)D(i\omega) \qquad (E6)$$

contains the expectation value of σ^z with respect to the π-flux state. Thus, we have to consider a matrix Green's function,

$$\underline{\mathbf{D}}(\boldsymbol{q}, i\omega) = \begin{pmatrix} \mathbf{D}_{11}(\boldsymbol{q}, i\omega) & \mathbf{D}_{12}(\boldsymbol{q}, i\omega) \\ \mathbf{D}_{21}(\boldsymbol{q}, i\omega) & \mathbf{D}_{22}(\boldsymbol{q}, i\omega) \end{pmatrix}, \qquad (E7)$$

where the unit cell is as in Fig. 7. The Fourier transform of Eq. (E6) in matrix notation is thus

$$\underline{\mathbf{D}}(\boldsymbol{q}, i\omega) = D(i\omega)\mathbf{1}_\gamma$$

$$+ 2JD(i\omega)[\cos(q_x)\gamma_x - \cos(q_y)\gamma_z]\underline{\mathbf{D}}(\boldsymbol{q}, i\omega) \quad (E8)$$

FIG. 13. Configurations of average flux $\Phi = \pi/2$ and associated fermionic ground-state energies as a function of filling.
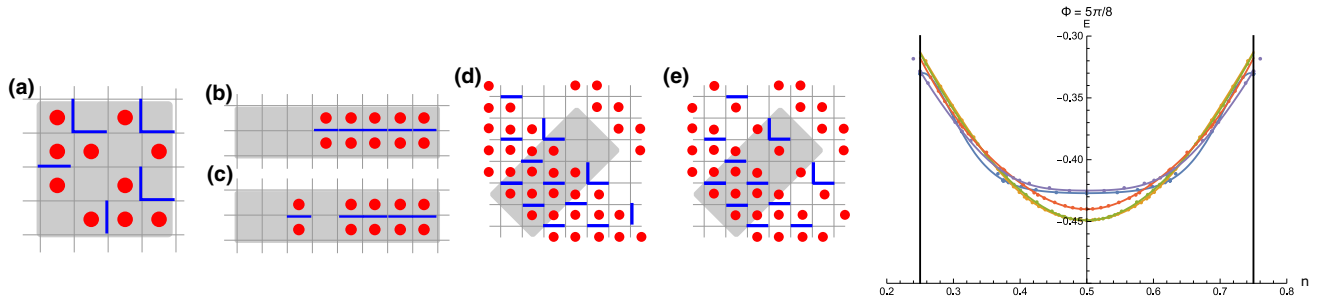
FIG. 14. Configurations of average flux $\Phi = 5\pi/8$ and associated fermionic ground-state energies as a function of filling.

and therefore

$$\underline{\mathbf{D}}(\mathbf{q}, i\omega) = 4h\{\omega^2 + 4h(h - 2J[\cos(q_x)\gamma_x - \cos(q_y)\gamma_z])\}^{-1}. \tag{E9}$$

This propagator has two transitions happening simultaneously: one at $\mathbf{q} = (0, 0)$ and one at $\mathbf{q} = (0, \pi)$ (recall that $\mathbf{q} \in$ $(-\pi/2, \pi/2) \times (-\pi, \pi)$). The inclusion of t implies a shift $J \to J + \bar{t}$ where $\bar{t} = 2t G_{\mathrm{FS}}(\mathbf{r}, \mathbf{r}'; \tau, \tau)$ and $\mathbf{r}, \mathbf{r}'$ are nearest neighbors.

b. Self-interaction of electric strings

The ϕ^4 theory for the π flux can be regarded as [$\vec{\phi} = (\phi_1, \phi_2)$ lives on the two basis sites of the unit cell, Fig. 7]

$$S[\vec{\phi}] = \int d\tau (dq)\vec{\phi}(-\mathbf{q}, \tau) \frac{[-\partial_\tau^2 + 4h(h - 2J[\cos(q_x)\gamma_x - \cos(q_y)\gamma_z])]}{2} \vec{\phi}(\mathbf{q}, \tau) + \frac{\lambda}{4!}[\phi_1(\mathbf{x}, \tau)^4 + \phi_2(\mathbf{x}, \tau)^4]. \tag{E10}$$

The locality of interactions in real space of Fig. 4(b) implies the $\phi_1^4 + \phi_2^4$ form of interactions and $\lambda \sim a^2 J^4/h$. To derive the critical theory, we diagonalize the quadratic term, the bottom of the band is near $q_x = 0$ and gapped, so it is sufficient to only consider the wave functions of the lower band. Then

$$S[\phi_0] = \int d\tau (dq)\phi_-(-\mathbf{q}, \tau) \frac{[-\partial_\tau^2 + 4h(h - 2J[\sqrt{\cos(q_x)^2 + \cos(q_y)^2}])]}{2} \phi_-(\mathbf{q}, \tau) + \frac{\lambda}{4!}[\phi_-(\mathbf{x}, \tau)^4]. \tag{E11}$$

A factor of order unity has been absorbed into λ. In a subsequent step, we expand near the position of the minima of the ϕ_- field: $\phi_-(\mathbf{x}, \tau) \simeq \phi_0(\mathbf{x}, \tau) + \phi_\pi(\mathbf{x}, \tau)e^{i\pi y}$, where both ϕ_0 and ϕ_π are slow fields. We group them into a complex field $\phi = \phi_0 + i\phi_\pi$ and obtain the effective theory (the relative weight of $\phi_0^4 + \phi_\pi^4$ and $\phi_0^2\phi_\pi^2$ follows from momentum conservation):

$$S[\phi] = \int d\tau d^2x \, \bar{\phi}[-\partial_\tau^2 - v^2\nabla^2 + 4h(h - 2J\sqrt{2}))]\phi$$
$$+ \frac{\lambda}{2}|\phi|^4. \tag{E12}$$

Again, we absorbed a factor of order one into λ.

We now discuss the real-space pattern of the condensed Higgs field ϕ assuming a parametrization $\phi_0 \sim \cos(\varphi)$, $\phi_\pi \sim \sin(\varphi)$, where φ is the XY angle which orders at the transition. Then, in a given unit cell,

$$\begin{pmatrix} \phi_1 \\ \phi_2 \end{pmatrix} \propto \cos(\varphi)\begin{pmatrix} \sqrt{2 - \sqrt{2}} \\ \sqrt{2 + \sqrt{2}} \end{pmatrix} + (-1)^y \sin(\varphi)\begin{pmatrix} \sqrt{2 + \sqrt{2}} \\ \sqrt{2 - \sqrt{2}} \end{pmatrix}, \tag{E13}$$

where the vector structure follows from the eigenstates of $\cos(q_x)\gamma_x - \cos(q_y)\gamma_z$ at $\mathbf{q} = 0$, $\mathbf{q} = (0, \pi)$. Translational invariance in x direction implies $\phi_1 = \phi_2$ and thus

$$\cos(\varphi) - (-1)^y \sin(\varphi) = 0, \tag{E14}$$

while additionally imposing translational symmetry in y direction implies that the equation shall be valid for any row y. This is impossible, therefore the Higgs field $(\phi_1, \phi_2)(\mathbf{x})$ always condenses in an inhomogeneous state, breaking the crystalline symmetries of the model.

c. Interaction between fermions and strings

To obtain the effective interaction of fermions and strings, we consider the microscopic interaction, Fig. 5 of the main text,

$$H_{\mathrm{int}} = t \sum_{\mathbf{r}} [c_1^\dagger(\mathbf{r})c_2(\mathbf{r})\phi_1(\mathbf{r})\phi_2(\mathbf{r})$$
$$+ c_2^\dagger(\mathbf{r})c_1(\mathbf{r} + 2\hat{e}_x)\phi_2(\mathbf{r})\phi_1(\mathbf{r} + 2\hat{e}_x)$$
$$+ c_1^\dagger(\mathbf{r})c_1(\mathbf{r} + \hat{e}_y)\phi_1(\mathbf{r})\phi_1(\mathbf{r} + \hat{e}_y)$$
$$+ c_2^\dagger(\mathbf{r})c_2(\mathbf{r} + \hat{e}_y)\phi_2(\mathbf{r})\phi_2(\mathbf{r} + \hat{e}_y)] + \mathrm{H.c.} \tag{E15}$$

We consider only the coupling to the critical modes, i.e.,

$$\vec{\phi}(\mathbf{x}) \simeq \phi_0(\mathbf{x})\frac{1}{\sqrt{4 - 2\sqrt{2}}}\begin{pmatrix} -1 + \sqrt{2} \\ 1 \end{pmatrix}$$
$$+ (-1)^y \phi_\pi(\mathbf{x})\frac{1}{\sqrt{4 - 2\sqrt{2}}}\begin{pmatrix} 1 \\ -1 + \sqrt{2} \end{pmatrix}. \tag{E16}$$
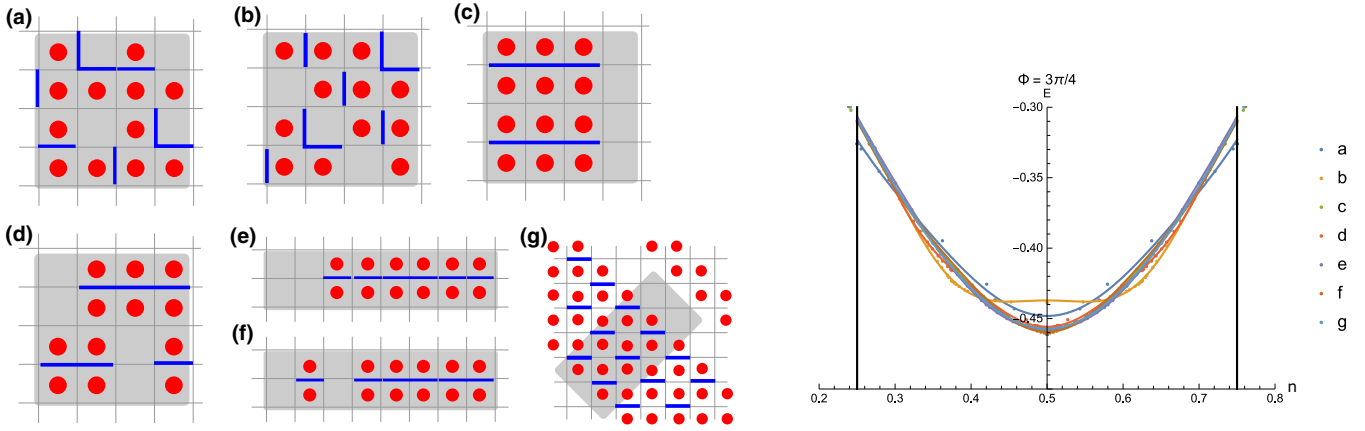
FIG. 15. Configurations of average flux $\Phi = 3\pi/4$ and associated fermionic ground-state energies as a function of filling.

Thus we obtain

$$\phi_1(\boldsymbol{r})\phi_2(\boldsymbol{r}) \simeq \frac{\phi_0^2 + \phi_\pi^2}{2\sqrt{2}} + (-1)^y \phi_0 \phi_\pi, \qquad \text{(E17)}$$

$$\phi_2(\boldsymbol{r})\phi_1(\boldsymbol{r} + 2\hat{e}_x) \simeq \frac{\phi_0^2 + \phi_\pi^2}{2\sqrt{2}} + (-1)^y \phi_0 \phi_\pi, \qquad \text{(E18)}$$

$$\phi_1(\boldsymbol{r})\phi_1(\boldsymbol{r} + \hat{e}_y) \simeq -\frac{\phi_0^2 + \phi_\pi^2}{2\sqrt{2}} + \frac{\phi_0^2 - \phi_\pi^2}{2}, \qquad \text{(E19)}$$

$$\phi_2(\boldsymbol{r})\phi_2(\boldsymbol{r} + \hat{e}_y) \simeq \frac{\phi_0^2 + \phi_\pi^2}{2\sqrt{2}} + \frac{\phi_0^2 - \phi_\pi^2}{2}. \qquad \text{(E20)}$$

We can now study the low-energy theory near the Dirac nodes, using the spinor $\psi = (\psi_{1,\pi/2}, \psi_{2,\pi/2}, \psi_{2,-\pi/2}, \psi_{2,-\pi/2})$, where 1,2 denotes the sublattice position and $\pm\pi/2$ the y coordinate in the Brillouin zone $(0, \pi) \times (-\pi, \pi)$). The effective kinetic Hamiltonian near the Dirac nodes takes the form

$$h(\boldsymbol{p}) = -w[p_x \gamma_x \mathbf{1}_\tau - p_y \gamma_y \tau_z]. \qquad \text{(E21)}$$

Interactions between fermions and critical electric strings are given by

$$S_{\text{int}} \sim a^2 t h \int d\tau d^2x \left\{ |\phi|^2 \bar{\psi} \left[\frac{h(-i\nabla)}{w} \right] \psi \right.$$
$$+ 2\sqrt{2}\phi_0\phi_\pi \bar{\psi}(-i\nabla_x)\tau_x\gamma_x\psi$$
$$\left. - \sqrt{2}[\phi_0^2 - \phi_\pi^2]\bar{\psi}(-i\nabla_y)\psi \right\}. \qquad \text{(E22)}$$

APPENDIX F: ANALOGUE QUANTUM COMPUTER USING MAJORANA COOPER PAIR BOXES

In this Appendix, we provide further details about the implementation of fermionic $\mathbb{Z}_2$ gauge theories using analog quantum computers based on Majorana Cooper pair boxes.

The basic building block, Figs. 6(b) and 9(a), to emulate the toric code sector of our model is a pair of MCBs. A standard setup for each such MCB (here 1 for top and 2 for bottom) consists of two Kitaev wires which are contacted to a mesoscopic superconductor. The whole box is capacitively coupled to the ground by $E_C(\hat{N}_{1,2} - N_0)^2$ (eigenvalues of $\hat{N}_{1,2}$ are integers, in this convention the condensate can absorb two units). The parity of the total number of electrons on the island

fixes the parity of the Majorana sector, e.g., $\alpha\beta\gamma\delta = -1$. In this subspace, we introduce Pauli-Matrices, see Ref. [50] and Fig. 9(a):

$$Z = i\alpha\beta \doteq i\gamma\delta, \qquad \text{(F1a)}$$

$$X = i\alpha\gamma \doteq i\delta\beta. \qquad \text{(F1b)}$$

We used the projector onto the low-energy subspace at $\doteq$. Hopping matrix elements, see Fig. 9(b), between the Majorana end modes at the wires and electrons in the dots are

$$H_\lambda = \lambda_{\gamma\alpha}\gamma_l\alpha_r e^{i\hat{\phi}_l/2 - i\hat{\phi}_r/2} + \text{H.c. [top part of Fig. (9(b))]}, \qquad \text{(F2)}$$

$$H_{\bar{\lambda}} = \bar{\lambda}\gamma_{rb}\delta_{br}e^{i\hat{\phi}_{rb}/2 - i\hat{\phi}_{br}/2} \text{ [bottom right of Fig. (9(b))]}, \qquad \text{(F3)}$$

$$H_t = t_{c^\dagger\alpha}c^\dagger\alpha e^{-i\hat{\phi}_r/2} + \text{H.c. [top right in Fig. (9(b))]}. \qquad \text{(F4)}$$

We will drop the subscript of matrix elements and assume $\bar{\lambda}$, λ and t to have the same amplitude everywhere as displayed in Fig. 9(b).

A pair of adjacent MCBs is coupled by superexchange processes $H_{\text{SX}} = 2|\lambda|^2 \cos(\Phi)Z_1Z_2/E_C$, such that for enclosed flux $\Phi < \pi/2$ the effective logical qubit states are $|\uparrow_1, \downarrow_2\rangle, |\downarrow_1, \uparrow_2\rangle$ and $\sigma^z = Z_1/2 - Z_2/2$, $\sigma^x = X_1X_2$. We project the toric code sector onto the logical, low-energy subspace, and obtain Eqs. (1) of the main text using perturbation theory [50,51]:

$$w \sim -|t|^2 \sin(\Phi/2)/E_C, \qquad \text{(F5)}$$

$$K \sim -|\bar{\lambda}|^4 \cos(\Phi_\square)/E_C^3, \qquad \text{(F6)}$$

$$h \sim \mathcal{C}_1|t|^2|\bar{\lambda}|^4|\lambda|^3/E_C^8 + \mathcal{C}_2|t|^6|\bar{\lambda}|^4/|\lambda|^3 E_C^6 \qquad \text{(F7)}$$

(with Φ dependent parameters $\mathcal{C}_{1,2}$). The impact of the star term without fermionic parity, which has a coupling

$$h' = \frac{|\bar{\lambda}|^4}{E_C^4}\left(\mathcal{C}_3\frac{|\lambda|^4}{E_C^3} - \mathcal{C}_4\frac{|t|^4}{E_C^3} - \mathcal{C}_5\frac{|t^2\bar{\lambda}|^4}{|\lambda|^6 E_C}\right), \qquad \text{(F8)}$$

can be mitigated by appropriate tuning of $|t/\lambda|$ since the dimensionless parameters $\mathcal{C}_{1,2,3,4,5}$ are positive for small flux Φ through a pair of MCBs.
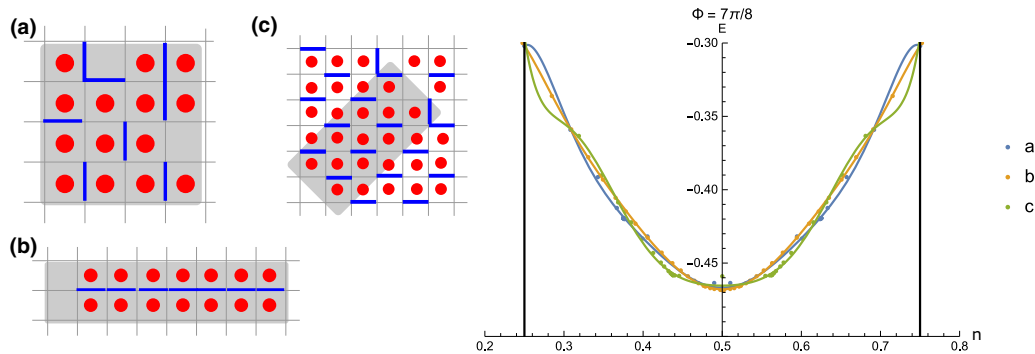
FIG. 16. Configurations of average flux $\Phi = 7\pi/8$ and associated fermionic ground-state energies as a function of filling.

APPENDIX G: OSM-OM TRANSITION: FLUX CONFIGURATIONS

In this Appendix, we present numerical details on the flux configurations underlying the transition from OSM to OM, as discussed in Sec. II B of the main text.

To illustrate the physics at the small to large Fermi surface transition, we numerically diagonalized the Hamiltonians associated to a variety of flux configurations with average flux $\Phi = k\pi/8$, $k = 0, \ldots, 8$ and determined fermionic energy $E_{c,\Phi}$ and particle density (=filling) n at temperature $T = w/100$, for system size 40×40, and chemical potential $E_F \in [-w, w]$ (step size $\Delta E_F = w/20$). Clearly, at $k = 0, 8$, simple analytical calculations could be used to check the numerical results. We subsequently fitted the numerical data to a symmetric eighth-order polynomial and thereby obtained

an approximate function $E_{c,\Phi}(n)$ for each of the 38 configurations. The chosen range of chemical potentials allows reliable fits within a density $n \in [0.25, 0.75]$. Finally, we determined the flux associated to the minimal total energy $E_{\text{tot}}(K, \rho) = \min_{\Phi, \text{config's}}[-K\Phi + 2E_{c,\Phi}(\rho)]$ and plotted it as a density plot in Fig. 1(b). We have explicitly checked that particle-hole-symmetry is present in the phase diagram and therefore only plot $n > 1/2$.

In Figs. 10–16, we summarize the considered flux configurations, along with the associated numerical data and fits of $E_{c,\Phi}(n)$. In the schematic pictures of the lattice, blue bonds represent hopping matrix elements $-w$ and red dots a π flux threading a plaquette. We considered three types of 16-site unit cells (shaded gray in the figures), thus the starting point of the numerics are the 16×16 momentum space matrix Hamiltonians.

[1] C. Proust and L. Taillefer, Annu. Rev. Condens. Matter Phys. **10**, 409 (2019).

[2] Q. Si and F. Steglich, Science **329**, 1161 (2010).

[3] Z. Xiang, Y. Kasahara, T. Asaba, B. Lawson, C. Tinsman, L. Chen, K. Sugimoto, S. Kawaguchi, Y. Sato, G. Li, S. Yao, Y. L. Chen, F. Iga, J. Singleton, Y. Matsuda, and L. Li, Science **362**, 65 (2018).

[4] G. Li, Z. Xiang, F. Yu, T. Asaba, B. Lawson, P. Cai, C. Tinsman, A. Berkley, S. Wolgast, Y. S. Eo, D.-J. Kim, C. Kurdak, J. W. Allen, K. Sun, X. H. Chen, Y. Y. Wang, Z. Fisk, and L. Li, Science **346**, 1208 (2014).

[5] B. S. Tan, Y.-T. Hsu, B. Zeng, M. C. Hatnean, N. Harrison, Z. Zhu, M. Hartstein, M. Kiourlappou, A. Srivastava, M. D. Johannes, T. P. Murphy, J.-H. Park, L. Balicas, G. G. Lonzarich, G. Balakrishnan, and S. E. Sebastian, Science **349**, 287 (2015).

[6] S. Yamashita, Y. Nakazawa, M. Oguni, Y. Oshima, H. Nojiri, Y. Shimizu, K. Miyagawa, and K. Kanoda, Nat. Phys. **4**, 459 (2008).

[7] M. Vojta, J. Low Temp. Phys. **161**, 203 (2010).

[8] S. Sachdev, Rep. Prog. Phys. **82**, 014001 (2018).

[9] P. Coleman, Phys. Rev. B **29**, 3035 (1984).

[10] L. de'Medici, A. Georges, and S. Biermann, Phys. Rev. B **72**, 205124 (2005).

[11] A. Rüegg, S. D. Huber, and M. Sigrist, Phys. Rev. B **81**, 155118 (2010).

[12] M. S. Scheurer, S. Chatterjee, W. Wu, M. Ferrero, A. Georges, and S. Sachdev, Proc. Natl. Acad. Sci. **115**, E3665 (2018).

[13] J. M. Luttinger, Phys. Rev. **119**, 1153 (1960).

[14] M. Oshikawa, Phys. Rev. Lett. **84**, 3370 (2000).

[15] T. Senthil, S. Sachdev, and M. Vojta, Phys. Rev. Lett. **90**, 216403 (2003).

[16] A. Paramekanti and A. Vishwanath, Phys. Rev. B **70**, 245118 (2004).

[17] A. Y. Kitaev, Quantum error correction with imperfect gates, in *Quantum Communication, Computing, and Measurement*, edited by O. Hirota, A. S. Holevo, and C. M. Caves (Springer US, Boston, MA, 1997), pp. 181–188.

[18] F. F. Assaad and T. Grover, Phys. Rev. X **6**, 041049 (2016).

[19] S. Gazit, M. Randeria, and A. Vishwanath, Nat. Phys. **13**, 484 (2017).

[20] S. Gazit, F. F. Assaad, S. Sachdev, A. Vishwanath, and C. Wang, Proc. Natl. Acad. Sci. **115**, E6987 (2018).

[21] J. S. Hofmann, F. F. Assaad, and T. Grover, Phys. Rev. B **100**, 035118 (2019).

[22] C. Chen, X. Y. Xu, Y. Qi, and Z. Y. Meng, Chin. Phys. Lett. **37**, 047103 (2020).

[23] S. Gazit, F. Assaad, and S. Sachdev, arXiv:1906.11250v1.

[24] C. Chen, T. Yuan, Y. Qi, and Z. Y. Meng, arXiv:2007.05543.

[25] E. J. König, P. Coleman, and Y. Komijani, arXiv:2002.12338.

[26] U. F. P. Seifert, T. Meng, and M. Vojta, Phys. Rev. B **97**, 085118 (2018).

[27] W. Choi, P. W. Klein, A. Rosch, and Y. B. Kim, Phys. Rev. B **98**, 155123 (2018).

[28] A. Kitaev, Ann. Phys. **321**, 2 (2006).

[29] M. Levin, F. J. Burnell, M. Koch-Janusz, and A. Stern, Phys. Rev. B **84**, 235145 (2011).

[30] Y. Zhong, Y.-F. Wang, and H.-G. Luo, Phys. Rev. B **88**, 045109 (2013).

[31] Z.-C. Gu, Z. Wang, and X.-G. Wen, Phys. Rev. B **90**, 085140 (2014).

[32] C. Prosko, S.-P. Lee, and J. Maciejko, Phys. Rev. B **96**, 205104 (2017).

[33] R. Nandkishore, M. A. Metlitski, and T. Senthil, Phys. Rev. B **86**, 045128 (2012).

[34] F. J. Wegner, J. Math. Phys. **12**, 2259 (1971).

[35] I. S. Tupitsyn, A. Kitaev, N. V. Prokof'ev, and P. C. E. Stamp, Phys. Rev. B **82**, 085114 (2010).

[36] E. Zohar, A. Farace, B. Reznik, and J. I. Cirac, Phys. Rev. Lett. **118**, 070501 (2017).

[37] A. Smith, J. Knolle, R. Moessner, and D. L. Kovrizhin, Phys. Rev. B **97**, 245137 (2018).

[38] J. Fu, J. Knolle, and N. B. Perkins, Phys. Rev. B **97**, 115142 (2018).

[39] Y. Hasegawa, P. Lederer, T. M. Rice, and P. B. Wiegmann, Phys. Rev. Lett. **63**, 907 (1989).

[40] P. A. M. Dirac, Proc. R. Soc. London, Ser. A **114**, 243 (1927).

[41] E. Fradkin and S. H. Shenker, Phys. Rev. D **19**, 3682 (1979).

[42] S. Trebst, P. Werner, M. Troyer, K. Shtengel, and C. Nayak, Phys. Rev. Lett. **98**, 070602 (2007).

[43] J. Vidal, S. Dusuel, and K. P. Schmidt, Phys. Rev. B **79**, 033109 (2009).

[44] S. Sachdev and T. Morinari, Phys. Rev. B **66**, 235117 (2002).

[45] Y. Zhong, K. Liu, Y.-Q. Wang, and H.-G. Luo, Phys. Rev. B **86**, 165134 (2012).

[46] E.-G. Moon and C. Xu, Phys. Rev. B **86**, 214414 (2012).

[47] T. Grover and T. Senthil, Phys. Rev. B **81**, 205102 (2010).

[48] L. Fu, Phys. Rev. Lett. **104**, 056402 (2010).

[49] B. Béri and N. R. Cooper, Phys. Rev. Lett. **109**, 156803 (2012).

[50] B. M. Terhal, F. Hassler, and D. P. DiVincenzo, Phys. Rev. Lett. **108**, 260504 (2012).

[51] L. A. Landau, S. Plugge, E. Sela, A. Altland, S. M. Albrecht, and R. Egger, Phys. Rev. Lett. **116**, 050501 (2016).

[52] E. König (unpublished).

[53] B. Keimer, S. A. Kivelson, M. R. Norman, S. Uchida, and J. Zaanen, Nature **518**, 179 (2015).

[54] E. Fradkin, *Field Theories of Condensed Matter Physics* (Cambridge University Press, Cambridge, UK, 2013).